Doctoral Dissertation

# Interplay between Checkerboard and Quasiparticle Interference Modulations in $Bi_2Sr_2CaCu_2O_{8+x}$

（$Bi_2Sr_2CaCu_2O_{8+x}$ におけるチェッカーボード変調と準粒子干渉変調の相互作用）

**Shusei Mizuta**

Department of Condensed Matter Physics,

Graduate School of Science, Hokkaido University

March 2021

# Abstract

In high-$T_c$ cuprate superconductors including $Bi_2Sr_2CaCu_2O_{8+x}$, it is well established that the $d$-wave superconductivity coexists with several kinds of electronic superstructures in the local density of states (LDOS). Above all, the checkerboard (CB) modulation of unknown microscopic origin has attracted much attention since its discovery by early scanning tunneling microscopy/spectroscopy (STM/STS) works. Recently, scanned-Josephson tunneling microscopy (SJTM) has detected a similar checkerboardlike pattern in the superfluid density, suggesting the presence of a pair density wave (PDW). This provides a question of whether such a PDW state can explain the CB modulation in the low-energy single-particle excitations measured by STM/STS.

In the low-energy region where the CB modulation manifests itself, quasiparticle interference (QPI) modulation arising from the scatterings of Bogoliubov quasiparticles is also observed. The probability of quasiparticle scatterings is characterized by the coherence factor that depends on the scattering process and the nature of scattering source. Therefore, QPI modulation can be used as a tool to detect a possible interplay between the SC quasiparticles and the CB modulation, and to identify the nature of the interplay (if any).

In this thesis, I will report on the spatial relationship between CB and QPI modulations coexisting in identical regions of the $CuO_2$ plane. After separating these two superstructures from each other, the local amplitude and phase are examined for the CB modulation and $\boldsymbol{q}_1$ component of QPI, which have similar wave vectors. The present study establishes a settled spatial phase relationship between CB and $\boldsymbol{q}_1$-QPI modulations, which tends to be realized where the CB modulation develops well, suggesting an interplay between CB and $\boldsymbol{q}_1$-QPI modulations. In light of this finding, the possible origin of CB modulation will be discussed.

# Acknowledgments

I would like to thank my supervisor Migaku Oda for his guidance of my research and for his help. I would like to thank Takafumi Kita, Atsushi Kawamoto and Noriaki Matsunaga for serving as examiners of my doctoral dissertation.

The research presented in this thesis was carried out in close collaboration with Tohru Kurosawa and Masayuki Ido whom I would like to thank for sharing their expertise in sample preparation and in STM/STS, as well as for valuable discussions.

Finally, I would like to thank all of my colleagues, past and present, for their help, as well as my family for their support and encouragement.

# Contents

# List of Figures

# List of Tables

# Chapter 1

# Introduction

Since the first discovery of high-$T_c$ cuprate superconductors in 1986 [1], a lot of efforts have been made to elucidate the mechanism of cuprate superconductivity. It is now well established that the cuprate superconductivity coexists with a mysterious pseudogap and various density wave states [2]. For the studies of density wave states, in particular, scanning tunneling microscopy/spectroscopy (STM/STS) probing the local density of states (LDOS) has played a crucial role. It has discovered several kinds of electronic superstructures that are supported by distinctive electronic states segregating the different momentum and/or energy regions on the Fermi surface.

## 1.1 Conventional Superconductors

A superconductor is a material where electrical resistivity vanishes [3] and magnetic flux is expelled from its bulk [4] below a critical temperature $T_c$. It is known today that these properties are based on the existence of many-particle condensate consisting of Cooper pairs of electrons whose wave function maintains phase coherence over macroscopic distances [5]. The electron pairing into a Cooper pair is allowed by the unstable Fermi surface against an infinitesimal attractive interaction between two electrons [6]. In the conventional superconductors including mercury, where the superconductivity was first discovered [3], the attractive interaction is provided by the electron-phonon coupling [7]. An electron moving through the crystal lattice attracts positively charged ions nearby itself. This results in a temporary positive charge accumulation of ions left behind, to which another electron with the opposite momentum and opposite spin is attracted. This spin-singlet pair $(\boldsymbol{k}\uparrow, -\boldsymbol{k}\downarrow)$ has a total momentum of $\boldsymbol{k}-\boldsymbol{k}=\boldsymbol{0}$. The scatterings of Cooper pairs condensed into the ground state without undergoing any excitation is indicative of the superfluidity of the pair with a charge $-2e$, or the superconductivity.

The excited states of this system are described by new fermionic operators introduced by Bogoliubov [8] and Valatin [9]

$$\gamma^\dagger_{\boldsymbol{k}0} = u^*_{\boldsymbol{k}} c^\dagger_{\boldsymbol{k}\uparrow} - v^*_{\boldsymbol{k}} c_{-\boldsymbol{k}\downarrow} \tag{1.1}$$

$$\gamma^\dagger_{\boldsymbol{k}1} = u^*_{\boldsymbol{k}} c^\dagger_{-\boldsymbol{k}\downarrow} + v^*_{\boldsymbol{k}} c_{\boldsymbol{k}\uparrow}, \tag{1.2}$$

where $c^\dagger_{\boldsymbol{k}\sigma}$ creates an electron with momentum $\boldsymbol{k}$ and spin $\sigma$. These quasiparticles created by operators $\gamma^\dagger_{\boldsymbol{k}0}$ and $\gamma^\dagger_{\boldsymbol{k}1}$ are called Bogoliubov quasiparticles. Equations 1.1 and 1.2 indicate that the Bogoliubov quasiparticles are a coherent superposition of electrons and holes. The coefficients

$$u_{\boldsymbol{k}} = \frac{1}{2}\sqrt{1+\frac{\varepsilon_{\boldsymbol{k}}}{E_{\boldsymbol{k}}}} \tag{1.3}$$

$$v_{\boldsymbol{k}} = \frac{1}{2}\sqrt{1-\frac{\varepsilon_{\boldsymbol{k}}}{E_{\boldsymbol{k}}}}\,e^{i\theta} \tag{1.4}$$

are called coherence factors. Their magnitudes $|v_{\boldsymbol{k}}|^2$ and $|u_{\boldsymbol{k}}|^2$ satisfying $|u_{\boldsymbol{k}}|^2+|v_{\boldsymbol{k}}|^2=1$ give the probabilities that the coherent pair state $(\boldsymbol{k}\uparrow, -\boldsymbol{k}\downarrow)$ with a common phase factor $e^{i\theta}$ is occupied and unoccupied, respectively. Here, $\varepsilon_{\boldsymbol{k}}$ is the normal-state band measured from the Fermi level and

$$E_{\boldsymbol{k}} = \sqrt{(\varepsilon^2_{\boldsymbol{k}} + |\Delta_{\boldsymbol{k}}|^2)} \tag{1.5}$$

is the excitation energy of the Bogoliubov quasiparticles with

$$\Delta_{\boldsymbol{k}} = |\Delta_{\boldsymbol{k}}|e^{i\theta} \tag{1.6}$$

being the $\boldsymbol{k}$-dependent superconducting order parameter. The excitation energy $E_{\boldsymbol{k}}$ takes on a minimum but finite value $|\Delta_{\boldsymbol{k}}|>0$ at the Fermi surface $\varepsilon_{\boldsymbol{k}}=0$, indicating the existence of an energy gap $|\Delta_{\boldsymbol{k}}|$. As the attractive interaction coming from the electron-phonon coupling is isotropic, the conventional superconductors exhibit an $s$-wave order parameter with

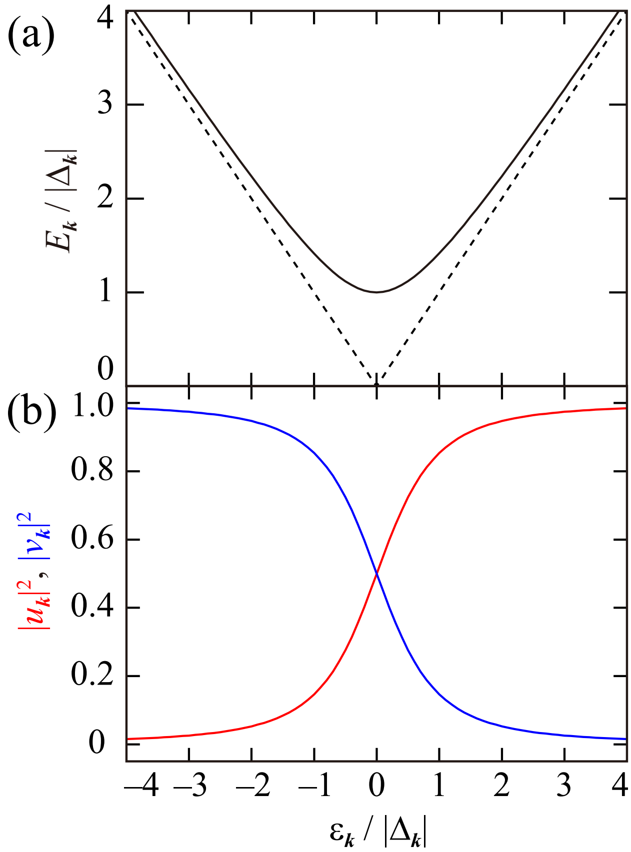


FIGURE 1.1: (a) Excitation energy of Bogoliubov quasiparticles $E_{\boldsymbol{k}}$ as a function of $\varepsilon_{\boldsymbol{k}}$. Dashed lines indicate $|\varepsilon_{\boldsymbol{k}}|$. (b) Quasiparticle proportions for electron- and hole-like components $|u_{\boldsymbol{k}}|^2$ and $|v_{\boldsymbol{k}}|^2$ as a function of $\varepsilon_{\boldsymbol{k}}$.

the same sign everywhere on the Fermi surface, leading to a fully gapped superconductivity.

## 1.2 High-$T_c$ Cuprate Superconductors

### 1.2.1 $d$-wave Superconducting Gap and Pseudogap

Another class of superconductors, called cuprate superconductors, has one or more $CuO_2$ planes in their layered crystal structures (see Fig. 2.1 for $Bi_2Sr_2CaCu_2O_{8+x}$). The high-$T_c$ superconductivity of unknown pairing mechanism occurs in these $CuO_2$ planes with doping holes. Below $T_c$, a superconducting (SC) gap with $d_{x^2-y^2}$ symmetry

$$\Delta_{\boldsymbol{k}} = \frac{\Delta_0}{2}(\cos k_x - \cos k_y) \tag{1.7}$$

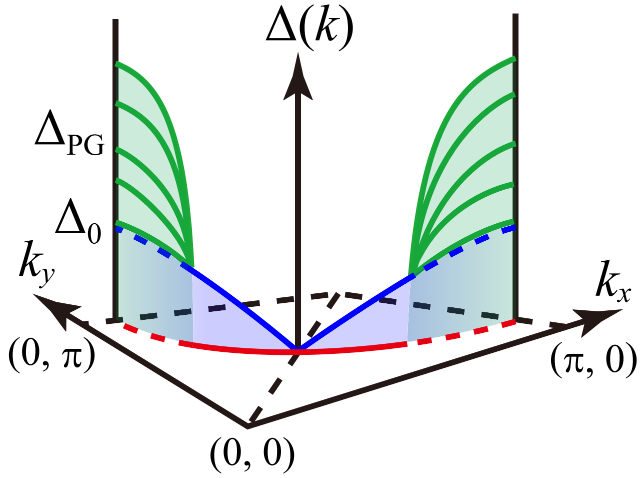


FIGURE 1.2: (a) Schematic of energy gaps at $T \leq T_{\rm c}$ on the Fermi surface. Since the two-dimensional Fermi surface of this system has $C_4$ symmetry, only a quarter of the first Brillouin zone is illustrated. Blue line indicates the superconducting gap with $d_{x^2-y^2}$ symmetry, and green one indicates the pseudogap, which opens at temperatures below $\sim T^*(> T_{\rm c})$. Opening of the pseudogap suppresses the quasiparticle DOS in the antinodal region near the zone boundary, truncating the normal-state Fermi surface (red line) into arc-shaped ones, called the Fermi arcs (solid red line). $\Delta_0$ indicates the $d$-wave SC gap amplitude, whereas $\Delta_{\rm PG}$ indicates spatially inhomogeneous pseudogap energy size.

opens. This $d$-wave SC gap undergoes an sign change by every $\pi/2$ in the momentum space, and has gapless points called nodes at diagonal directions. In the antinodal region near the zone boundary, a pseudogap develops at a temperature below $T^*(> T_{\rm c})$, leading to a suppression of the low-energy quasiparticle DOS there [10–16]. The successive normal-state Fermi surface is then truncated into arc-shaped one, called the Fermi arcs, around which the $d$-wave SC gap opens below $T_{\rm c}$. According to the nature of the quasiparticles living, the Fermi surface is roughly divided into two parts: nodal and antinodal regions. This dichotomy of the Fermi surface is one of the most striking features of the cuprate superconductivity [11–13, 17–22].

However, the relationship between nodal and antinodal electronic states is still elusive. Observations by the angle-resolved photoemission spectroscopy (ARPES) on a segregation of the nodal SC gap and the antinodal pseudogap is suggestive of a competitive relationship between them [11, 12]. On the other hand, time-resolved pump-probe optical spectroscopy has demonstrated a clear time correlation between the recovery processes of the SC and pseudogap states. After their complete destruction in a region several tens of $\mu$m in diameter, the recovery of the superconductivity seems to occur followed by that of the pseudogap. This is suggestive of an essential role of the pseudogap in the development of superconductivity [23].

### 1.2.2 Electronic Superstructures

Another clue to understand the relationship between nodal and antinodal states could be provided by electronic superstructures they host. Thus far, STM/STS has probed several types of electronic superstructures in the $CuO_2$ plane, which are specific to the nodal and antinodal states.

In the nodal region, where the $d$-wave SC gap opens, Bogoliubov quasiparticles scattered off some sources undergo quantum interferences. This leads to a DOS modulation called the quasiparticle interference (QPI) modulation [24–32].

In the antinodal region, electronic states seem to form two types of superstructures. At around the pseudigap energy $\Delta_{PG}$, unconventional charge density wave (CDW) breaking $C_4$ rotational symmetry within $CuO_2$ unit cells is observed. This CDW having modulations in antiphase on the $x$- and $y$-directed O sites ($x$ and $y$ label two orthogonal Cu-O bond directions) and no modulation on the Cu sites are called the $d$-symmetry form factor density wave ($d$FF-DW) [33–41]. On the other hand, at energies similar to or smaller than the SC gap amplitude $\Delta_0$, a checkerboard (CB) modulation [42–55] seemingly hosted by the residual antinodal states is observed. These two superstructures both run along the two orthogonal Cu-O bond directions, having similar characteristic wave vectors.

In this thesis, the spatial relationship between nodal QPI and antinodal CB modulations is investigated.

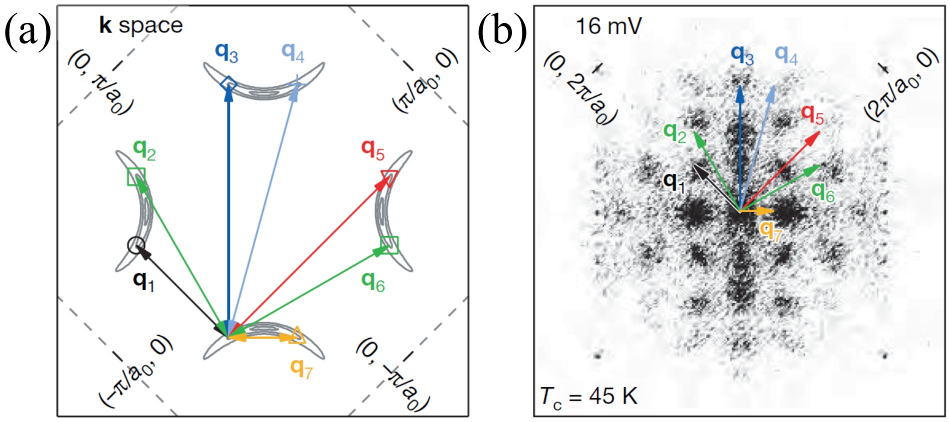


FIGURE 1.3: (a) Constant-energy contours of the $d$-wave Bogoliubov quasiparticle dispersion (solid gray lines). Open symbols indicate the tips of banana-shaped constant-energy contours, and double arrows indicate the seven independent scattering vectors $\boldsymbol{q}_1$–$\boldsymbol{q}_7$. (b) Observed $\boldsymbol{q}$-space structure of QPI modulation in underdoped $Bi_2Sr_2CaCu_2O_{8+x}$ exhibiting Fourier spots at $\boldsymbol{q}_1$–$\boldsymbol{q}_7$ [27].

## 1.3 Quasiparticle Interference (QPI) Modulation

When Bloch waves of quasiparticles are scattered off some sources, the scattered and incident waves having wave vectors $\boldsymbol{k}'$ and $\boldsymbol{k}$ undergo quantum interference. This gives rise to a stationary wave in quasiparticle LDOS at the wave vector $\boldsymbol{q} = \boldsymbol{k}' - \boldsymbol{k}$. This is called the QPI modulation [56, 57].

### 1.3.1 The Octet Model

In cuprates, QPI modulation is hosted by the Bogoliubov quasiparticles in the nodal region, where the $d$-wave SC gap $\Delta_{\boldsymbol{k}}$ opens. As shown in Fig. 1.3(a), the dispersion of these superconducting quasiparticles $E_{\boldsymbol{k}}$ has banana-shaped constant-energy contours, allowing elastic scatterings between any two states on them. However, the quasiparticle scatterings frequently occur between eight tips of bananas in the first Brillouin zone since the quasiparticle DOS

$$n_{\boldsymbol{k}}(E) \propto \frac{1}{|\nabla_{\boldsymbol{k}} E_{\boldsymbol{k}}|} \tag{1.8}$$

takes on maximum values there. The observed QPI modulation consists of seven independent components with scattering vectors

$$\boldsymbol{q}_1 = (2k_x, 0) \tag{1.9}$$
$$\boldsymbol{q}_2 = (k_x + k_y, k_y - k_x) \tag{1.10}$$
$$\boldsymbol{q}_3 = (k_x + k_y, k_y + k_x) \tag{1.11}$$
$$\boldsymbol{q}_4 = (2k_x, 2k_y) \tag{1.12}$$
$$\boldsymbol{q}_5 = (0, 2k_y) \tag{1.13}$$
$$\boldsymbol{q}_6 = (k_x - k_y, k_y + k_x) \tag{1.14}$$
$$\boldsymbol{q}_7 = (k_x - k_y, k_y - k_x), \tag{1.15}$$

where $\boldsymbol{k} \equiv (k_x, k_y)$ gives the position of a banana tip in momentum space at a given energy [24, 25]. Since the banana tips $\boldsymbol{k}$ trace the locus of the Bogoliubov band-minima, the dispersion relation of Bogoliubov quasiparticles $\boldsymbol{k}(E)$ can be known from an energy dependence of the observed QPI wave vectors $\boldsymbol{q}_i(E)$ [24–29].

### 1.3.2 Coherence Factor Effects

As the Bogoliubov quasiparticles are a coherent superposition of excitations of electrons and holes, the rates of quasiparticle scatterings are characterized by combinations of coefficients $u_{\boldsymbol{k}}$ and $v_{\boldsymbol{k}}$ [58, 59]. The detailed forms of the coherence factors in determining the probabilities of quasiparticle scatterings off some common scatterers are shown in Table 1.1 [60–64]. The dominant contributions for weak scalar, resonant and Andreev scatterers are given by

$$C_{\mathrm{s}}(\boldsymbol{k}, \boldsymbol{k'}) = (u_{\boldsymbol{k}} u_{\boldsymbol{k'}} - v_{\boldsymbol{k}} v_{\boldsymbol{k'}})^2 \tag{1.16}$$
$$C_{\mathrm{r}}(\boldsymbol{k}, \boldsymbol{k'}) = (u_{\boldsymbol{k}} u_{\boldsymbol{k'}} + v_{\boldsymbol{k}} v_{\boldsymbol{k'}})^2 \tag{1.17}$$
$$C_{\mathrm{a}}(\boldsymbol{k}, \boldsymbol{k'}) = (u_{\boldsymbol{k}} u_{\boldsymbol{k'}} + v_{\boldsymbol{k}} v_{\boldsymbol{k'}})(u_{\boldsymbol{k}} v_{\boldsymbol{k'}} + v_{\boldsymbol{k}} u_{\boldsymbol{k'}}) \propto \Delta_{\boldsymbol{k}} + \Delta_{\boldsymbol{k'}}, \tag{1.18}$$

respectively. The values of coherence factors $C(\boldsymbol{k}, \boldsymbol{k'})$ significantly change depending on whether the sign of order parameter $\Delta_{\boldsymbol{k}}$ is preserved or reversed between initial and final states of the scatterings because $v_{\boldsymbol{k}}$ has the same sign as the order parameter $\Delta_{\boldsymbol{k}}$, while $u_{\boldsymbol{k}}$ is always positive. For sign preserving scatterings at $\boldsymbol{q}_1$, $\boldsymbol{q}_4$ and $\boldsymbol{q}_5$ [Fig 1.4(a)], $C_{\mathrm{r}}(\boldsymbol{k}, \boldsymbol{k'})$ and $C_{\mathrm{a}}(\boldsymbol{k}, \boldsymbol{k'})$ take on finite values, whereas $C_{\mathrm{s}}(\boldsymbol{k}, \boldsymbol{k'})$ are strongly suppressed, and vice versa for sign-reversing scatterings at $\boldsymbol{q}_2$, $\boldsymbol{q}_3$, $\boldsymbol{q}_6$ and $\boldsymbol{q}_7$. Therefore, the intensities at sign-

| $T$ matrix | Scatterer | $C(q)$ in $R^{even}(\mathbf{q}, V)$ | $C(q)$ in $R^{odd}(\mathbf{q}, V)$ | Enhanced $q_i$ | Enhances "++"? |
|---|---|---|---|---|---|
| $\tau_3$ | Weak scalar | $(uu' + vv')(uu' - vv')$ | $(\mathbf{uu'} - \mathbf{vv'})^2$ | 2,3,6,7 | No |
| $\boldsymbol{\sigma} \cdot \mathbf{m}$ | Weak magnetic | 0 | 0 | None | No |
| $i$ sgn $\omega$ $\hat{\mathbf{1}}$ | Resonant | $(\mathbf{uu'} + \mathbf{vv'})^2$ | $(uu' + vv')(uu' - vv')$ | 1,4,5 | Yes |
| $\tau_1$ | Andreev | $(\mathbf{uu'} + \mathbf{vv'})(\mathbf{uv'} + \mathbf{vu'})$ | $(uu' - vv')(uv' + vu')$ | 1,4,5 | Yes |

TABLE. 1.1: Coherence factors $C(q)$ in $R^{even}(\boldsymbol{q}, V)$ and $R^{odd}(\boldsymbol{q}, V)$ for some common scatterers. $R^{even}(\boldsymbol{q}, V)$ and $R^{odd}(\boldsymbol{q}, V)$ are the even and odd density-density correlators. The dominant contribution for a particular type of scatterer is given in bold [64].

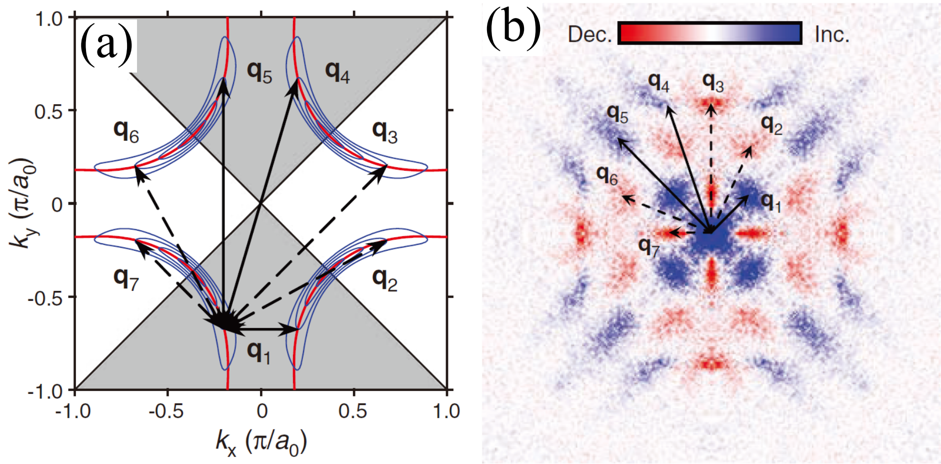


FIGURE 1.4: (a) Constant-energy contours of the $d$-wave Bogoliubov quasiparticle dispersion (blue lines) and resultant $\boldsymbol{q}_i$ vectors of QPI (double arrows). The order parameter $\Delta_{\boldsymbol{k}}$ exhibits opposite signs between white and shaded regions, resulting in a classification into sign-preserving scatterings ($\boldsymbol{q}_1$, $\boldsymbol{q}_4$ and $\boldsymbol{q}_5$) and sign-reversing scatterings ($\boldsymbol{q}_2$, $\boldsymbol{q}_3$, $\boldsymbol{q}_6$ and $\boldsymbol{q}_7$). Red lines denote the normal-state Fermi surface. (b) Difference of the $\boldsymbol{q}$-space intensity of QPI in $Ca_{2-x}Na_xCuO_2Cl_2$ ($x \sim 0.14$ and $T_c \sim 28$ K) between $B$ = 11 T and $B$ = 0 T. The intensities at sign-preserving $\boldsymbol{q}_i$ vectors ($\boldsymbol{q}_1$, $\boldsymbol{q}_4$ and $\boldsymbol{q}_5$) are enhanced by a field, whereas those at sign-reversing $\boldsymbol{q}_i$ vectors ($\boldsymbol{q}_2$, $\boldsymbol{q}_3$, $\boldsymbol{q}_6$ and $\boldsymbol{q}_7$) are suppressed [31].

preserving $\boldsymbol{q}_i$ vectors are enhanced by resonant or Andreev scatterers, while those at sign-reversing $\boldsymbol{q}_i$ vectors are enhanced by weak scalar scatterers (Table 1.1).

Thus far, coherence factor effects have been confirmed in $Ca_{2-x}Na_xCuO_2Cl_2$ and $Bi_2Sr_2CaCu_2O_{8+x}$ with applying a magnetic field, which introduces vortices as resonant and/or Andreev scatterers [31,32]. As shown in Fig. 1.4(b), the intensities at sign-preserving $\boldsymbol{q}_1$, $\boldsymbol{q}_4$ and $\boldsymbol{q}_5$ are enhanced in a magnetic field, whereas those at sign-reversing $\boldsymbol{q}_2$, $\boldsymbol{q}_3$, $\boldsymbol{q}_6$ and $\boldsymbol{q}_7$ are depressed. The depression of sign-reversing $\boldsymbol{q}_i$ vectors can be explained in terms of a uniform smearing effect on all QPI peaks due to the superflow around vortices [31, 63]. On the other hand, the momentum selective enhancement of the sign-preserving $\boldsymbol{q}_i$ vectors is attributed to the coherence factor effects described above.

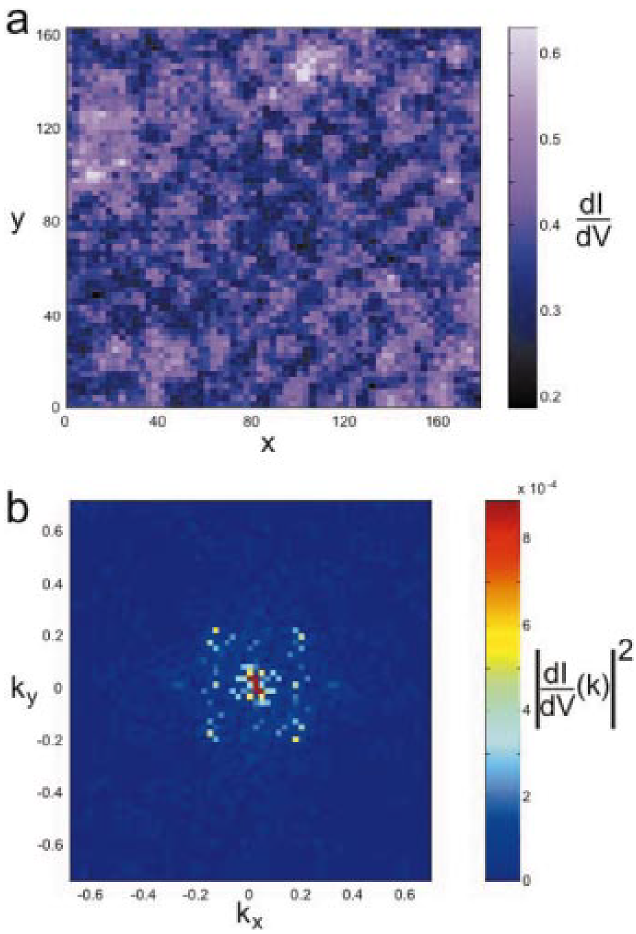


FIGURE 1.5: (a) Spatial map of $dI/dV$ of slightly overdoped $Bi_2Sr_2CaCu_2O_{8+x}$ ($T_c$ = 86 K) for $V_s$ = +15 mV. CB modulation along the two Cu-O-Cu directions (diagonal directions) are observed. (b) Power spectrum of the FT of (a) exhibiting two independent Fourier peaks of the CB modulation [43].

## 1.4 Checkerboard (CB) Modulation

Checkerboard (CB) modulation is an electronic superstructure that runs along the two orthogonal Cu-O bond directions with an energy-independent periodicity [42–55]. The CB modulation was first discovered around the vortex cores in $Bi_2Sr_2CaCu_2O_{8+x}$ [42]. Later, it was also found in the pure SC state of $Bi_2Sr_2CaCu_2O_{8+x}$, $Bi_{2-y}Pb_ySr_{2-z}La_zCuO_{6+x}$ and $Ca_{2-x}Na_xCuO_2Cl_2$ [43–45], and in the pseudogap state above $T_c$ [46].

Figure 1.5(a) shows a CB modulation reported by Howald *et al.* in 2003 [43].

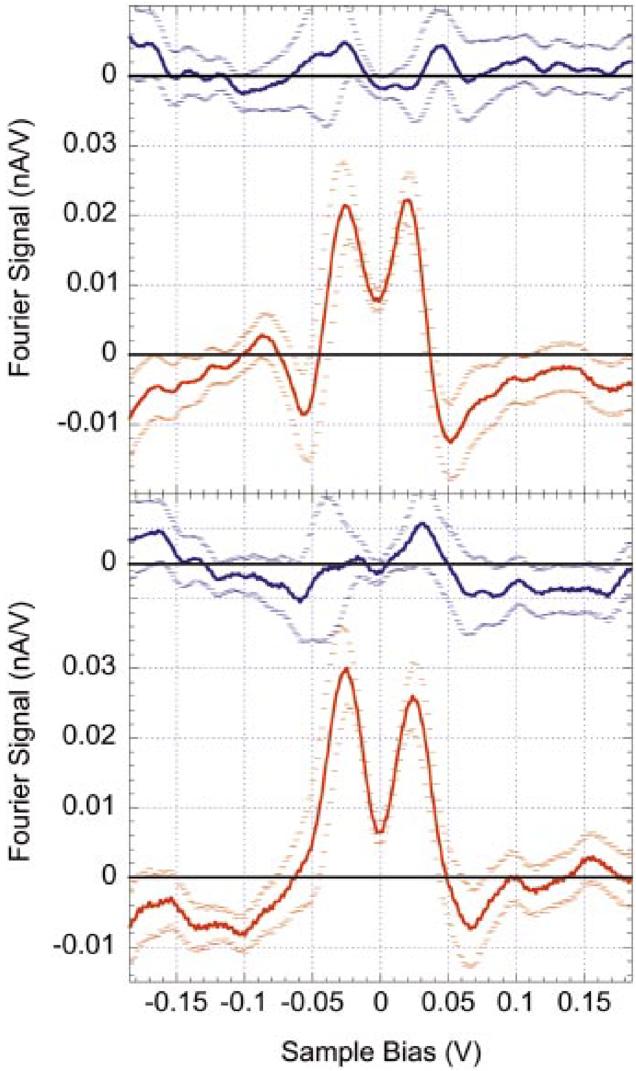


FIGURE 1.6: FT signals at $(\pm 0.25, 0) \times (2\pi/a)$ (top) and $(0, \pm 0.25) \times (2\pi/a)$ (bottom) as a function of $V_\mathrm{s}$. The red and blue lines indicate the real and imaginary parts, where the arbitrary phase were chosen to minimize the imaginary part [43].

The spatial map of the differential conductance $dI/dV$ reflecting the LDOS exhibits a checkerboardlike pattern along the two Cu-O bond directions (diagonal directions) with a periodicity of $\sim 4a$ ($a$: Cu-O-Cu distance). This yields the peaks at $(\pm 0.25, 0) \times (2\pi/a)$ and $(0, \pm 0.25) \times (2\pi/a)$ in the corresponding Fourier transform (FT) map [Fig. 1.5(b)]. Figure 1.6 shows the FT signals at these wave vectors as a function of the sample bias voltage $V_\mathrm{s}$ corresponding to the quasiparticle energy relative to the Fermi energy. The real part plotted in red, with a considerably smaller imaginary part plotted

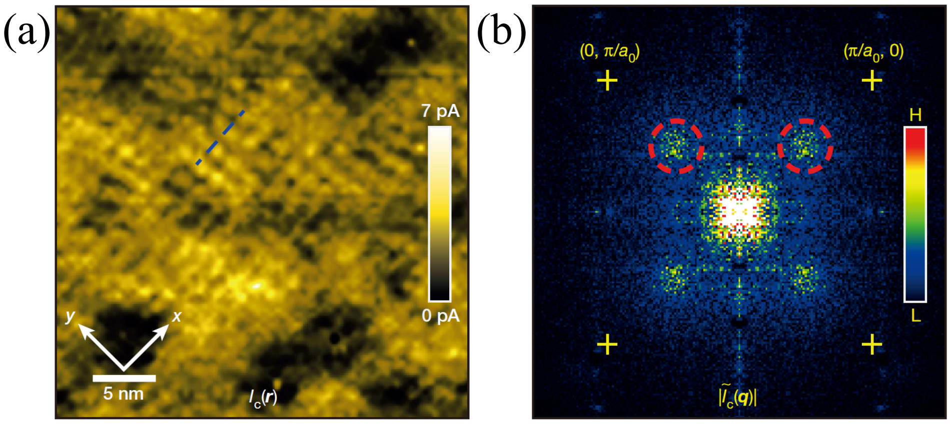


FIGURE 1.7: (a) Spatial map of the Josephson critical current of optimally doped $Bi_2Sr_2CaCu_2O_{8+x}$ ($p \sim 0.17$) exhibiting a PDW along the two Cu-O bond directions ($x$ and $y$ axes). (b) FT of (a). Dashed red circles indicate Fourier spots of the PDW at $(0.25, 0) \times (2\pi/a)$ and $(0, 0.25) \times (2\pi/a)$ [77].

in blue, shows the presence of CB modulation with a static phase for energy within a low-energy region $e|V_s| \leq 40$ meV $\sim \Delta_0$. Furthermore, maximum intensities of the CB modulation appear at $e|V_s| = 25$ mV $\sim \Delta_{SG}$, where $dI/dV$ spectra exhibit sub gaps. This early observation is indicative of the particle-hole symmetric nature of the nondispersive CB modulation, that is, its amplitude and phase of being almost symmetric with respect to the sign change of the bias voltage. A similar behavior is also confirmed in optimally doped $Bi_2Sr_{1.7}Eu_{0.3}CuO_{6+x}$ [55].

## 1.5 Pair Density Wave (PDW)

Pair density wave (PDW) is a state where spin-singlet Cooper pairing between Zeeman-split Fermi surfaces produces pairs with a finite momentum $\boldsymbol{Q}$, resulting in a spatially modulated pairing amplitude at this wave vector [65, 66]. For cuprates, theoretical works have proposed several types of PDWs to be the origin of the CB modulation [67–76]. Recently, scanned-Josephson tunneling microscopy (SJTM) has discovered a checkerboardlike spatial modulation in the superfluid density [77], suggesting the existence of a PDW in cuprates [78–81].

### 1.5.1 PDW Detected by SJTM

The first direct observation of PDW was achieved in optimally doped $Bi_2Sr_2CaCu_2O_{8+x}$ with a hole doping level of $p \sim 0.17$ by SJTM [77]. In this technique, an STM tip with a nanometer-sized flake of superconducting $Bi_2Sr_2CaCu_2O_{8+x}$ adhering is utilized. Then, the tunneling of Cooper pairs between a superconducting tip and a superconducting sample is used to image the spatial dependence of Josephson critical current, which is proportional to the superfluid density. As shown in Fig. 1.7, the superfluid density exhibits a checkerboardlike pattern, which is suggestive of a PDW state. The PDW runs along the two orthogonal Cu-O bond directions with a period of $\sim 4a$, and thus its wave vector is similar to those of $d$FF-DW and CB modulation.

### 1.5.2 PDW Detected by STM/STS

Subsequent to the SJTM work, Ruan *et al.* suggested that the signatures of PDW appear also in the low-energy single-particle excitations measured by the conventional STM/STS [82]. For visualizing the PDW in the SC state of heavily underdoped $Bi_2Sr_2CaCu_2O_{8+x}$ with $p \sim 0.06$ ($T_c = 10$ K), they proposed two key characteristics in the single-particle tunneling spectrum [Fig. 1.8(a)]. One is the amplitude of the coherence peak near the SC gap edge. This is based on the empirical positive correlation between the SC coherence and superfluid density [27, 77, 83–86]. The other is the depth of SC gap reflecting the gapping out of low-energy DOS due to the Cooper pairing.

To extract the spatial variation of the coherence peak amplitude, the negative of the second derivative of $dI/dV$ curve

$$D(\boldsymbol{r}, V_s) \equiv -\frac{\partial^2}{\partial V_s^2}\frac{\partial I(\boldsymbol{r}, V_s)}{\partial V_s} = -\frac{\partial^3 I(\boldsymbol{r}, V_s)}{\partial V_s^3} \tag{1.19}$$

was introduced, where $\boldsymbol{r} = (x, y)$ denotes the real-space coordinate. As can be seen in Fig. 1.8(c), $D$ curves exhibit peaks around $V_s = \pm 20$ mV, where

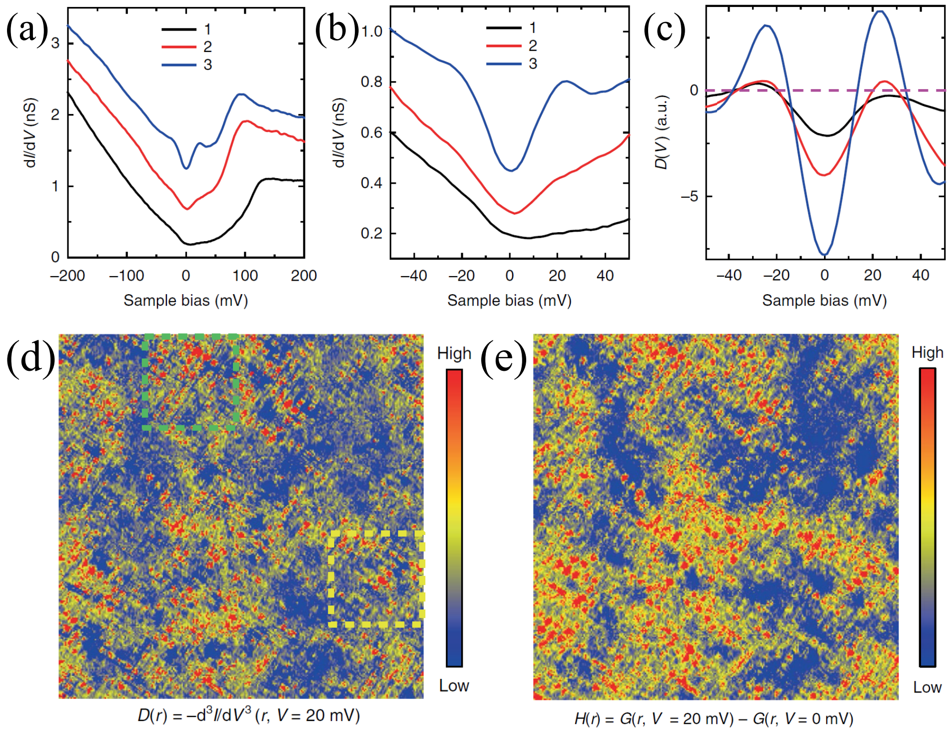


FIGURE 1.8: (a) Three typical $dI/dV$ spectra measured in heavily underdoped $Bi_2Sr_2CaCu_2O_{8+x}$ ($p \sim 0.06$ and $T_c = 10$ K), which exhibit the pseudogap at ∼100 mV and the SC gap (sub gap) at ∼20 mV. (b) The low-bias data of (a). (c) Negative of second derivative $D$ of (b). Feature of the SC coherence peak is enhanced. (d) $D(\boldsymbol{r}, V_s = +20$ mV$)$ map exhibiting a checkerboardlike pattern of the Cooper-pair density. (e) $H(\boldsymbol{r})$ map exhibiting a similar checkerboardlike pattern [82].

the $dI/dV$ curves exhibit sub gaps. Mathematically, the peak height at $V_s \sim \pm 20$ mV in $D$ curve reflects the curvature of the sub gap in the $dI/dV$ curve, or the sharpness of the SC coherence peak.

On the other hand, the depth of SC gap was defined by the difference between the sub-gap peak height at $V_s = +20$ mV and the gap bottom at $V_s = 0$ mV in the $dI/dV$ curve,

$$H(\boldsymbol{r}) \equiv \left.\frac{\partial I(\boldsymbol{r}, V_s)}{\partial V_s}\right|_{V_s=+20\ \mathrm{mV}} - \left.\frac{\partial I(\boldsymbol{r}, V_s)}{\partial V_s}\right|_{V_s=0\ \mathrm{mV}}. \tag{1.20}$$

The gap height $H$ reflects the low-energy quasiparticle DOS that is gapped out due to the Cooper pairing, and thus is expected to give the local pair density.

As shown in Figs. 1.8(d) and 1.8(e), the $D(\boldsymbol{r}, V_\mathrm{s} = +20\ \mathrm{mV})$ and $H(\boldsymbol{r})$ maps both exhibit a checkerboardlike pattern, which is indicative of a PDW. The PDW is positively correlated with the CB modulation observed in the low-energy STM images, suggesting a coexistence of PDW and CDW.

## 1.6 Organization of this Thesis

As presented in the preceding sections, understanding the origin of CB modulation in relation to the mechanism of superconductivity is one of the long-standing issues in the research field of cuprate superconductivity. The recent direct observation of PDW with a checkerboardlike pattern by SJTM [77] and the suggestion of PDW signatures found in the single-particle tunneling spectrum [82] provide a question of whether such PDW state can explain the CB modulation observed by STM/STS.

In this thesis, I utilize the QPI modulation arising from the scatterings of Bogoliubov quasiparticles as an indicator to detect a possible interplay between the SC quasiparticles and the CB modulation, and to identify the nature of the interplay (if any) according to the coherence factor effects. For this purpose, the spatial relationship between the CB and QPI modulation is investigated in the SC state ($T = 7$ K) of $\mathrm{Bi_2Sr_2CaCu_2O_{8+x}}$ with a hole doping level of $p \sim 0.12$ ($T_\mathrm{c} = 76$ K) near $p = 1/8$, around which the CB modulation develops markedly [51].

In Chapter 2, I describes the procedures of sample preparation and the experimental techniques relating to STM/STS.

In Chapter 3, I discuss the spatial relationship between CB and QPI modulations. As these two superstructures are both observed in the low-energy states, they are expected to be superimposed in the low-energy LDOS. This leads us to begin with the disentanglement of CB and QPI modulations, which will be detailed in Section 3.1. In Section 3.2, the local amplitude and phase are established for the CB modulation and $\boldsymbol{q}_1$ component of QPI, which have similar wave vectors, to investigate the local feature of each modulation by itself. In Section 3.3, I detail the spatial relationship between CB and $\boldsymbol{q}_1$-QPI modulations. This leads to a discussion on a possible interplay between the two superstructures and on the origin of the CB modulation.

In Chapter 4, I will summarize the results and conclusions of this thesis.

# Chapter 2

# Experimental Procedures

In the present research, STM/STS measurements were performed on single crystals of $Bi_2Sr_2CaCu_2O_{8+x}$, which have a layered crystal structure consisting of BiO, SrO, $CuO_2$ and Ca planes, as shown in Fig. 2.1. The crystal naturally cleaves between two BiO planes, where van der Waals-type bonding is present. In STM/STS measurements, single crystals were cleaved *in situ* in an ultrahigh vacuum at 7 K just before approaching the STM tip towards the sample surface. STM allows exploring the electronic states in the $CuO_2$ plane buried under semiconducting BiO and insulating SrO planes.

## 2.1 Sample Preparation

The single crystals of $Bi_2Sr_2CaCu_2O_{8+x}$ used in this study were grown from polycrystalline rods by using the traveling solvent floating zone (TSFZ) method [87, 88].

### 2.1.1 Weighing and Mixing

The polycrystal of $Bi_2Sr_2CaCu_2O_{8+x}$ was synthesized from dried powders of $Bi_2O_3$, $SrCO_3$, $CaCO_3$, and CuO with a purity of 99.99%. They were weighed to satisfy the composition $Bi_{2.2}Sr_{1.633}Ca_{1.166}Cu_2O_{8+x}$, and mixed well using agate mortar and pestle. The oxygen atoms are provided from atmospheric gas in courses of calcination, sintering and crystal growth by TSFZ described below. The amount of excess oxygen $x$, which determines the hole doping level of the sample, can be controlled by changing the oxygen partial pressure in the atmospheric gas.

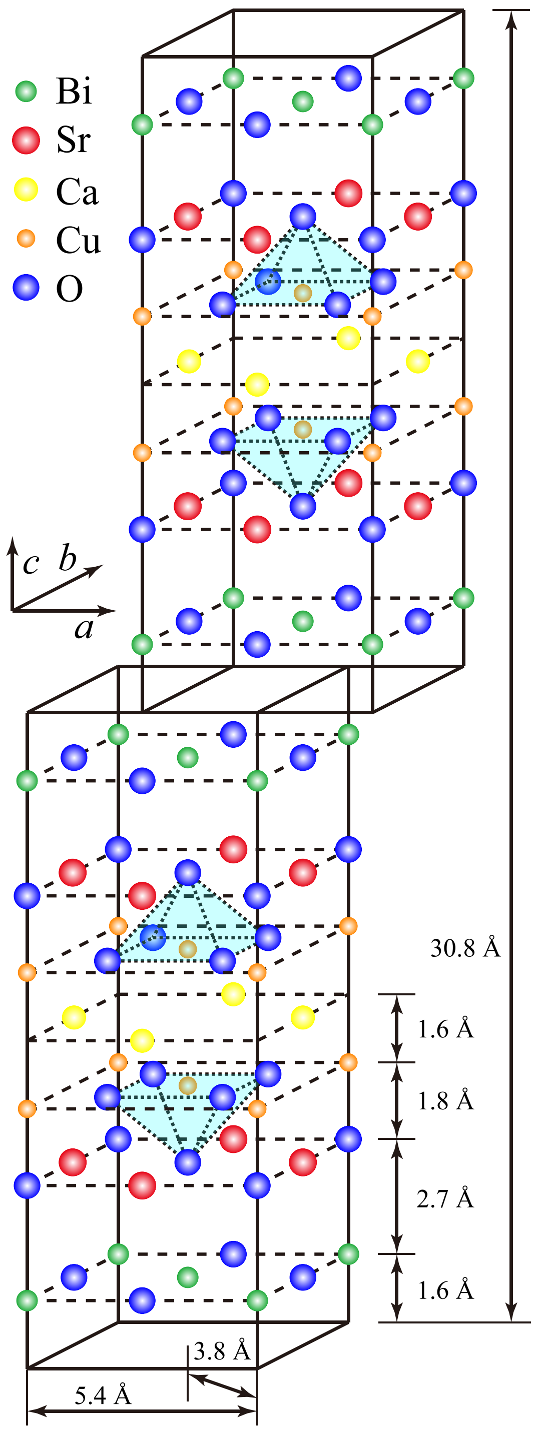


FIGURE 2.1: Unit cell of the cuprate superconductor $Bi_2Sr_2CaCu_2O_{8+x}$. The $CuO_2$ planes are sandwiched between BiO, SrO and Ca planes. The crystal exhibits an incommensurate structural buckling along the $b$ axis with a periodicity of $\sim$4.7 unit cells. This one-dimensional structural superlattice arises from a lattice mismatch between BiO and $CuO_2$ planes.

### 2.1.2 Calcination and Grinding

The raw material powder was then calcined several times at a temperature of 750–800°C for 24 h in an oxygen atmosphere using a tube furnace. The calcined body was ground using agate mortar and pestle after each calcination. Usually, the second and subsequent calcinations are made at a higher temperature than the preceding one. The hole doping level was controlled by changing both the oxygen partial pressure in the atmospheric gas and the calcination temperature.

### 2.1.3 Sintering

After grinding the calcined body, it was filled in a rubber tube with a diameter of 5 mm, and hydrostatically pressed up to ∼100 MPa to obtain a pressed rod with a length of ∼70 mm. The pressed rods were then sintered several times in an oxygen atmosphere using a tube furnace. Each sintering was made for 24 h at a temperature higher than the preceding calcination or sintering.

### 2.1.4 Crystal Growth by TSFZ Method

The objective single crystals were grown from the polycrystalline rods by using the TSFZ method (Fig. 2.2). A polycrystalline rod, or a feed rod is hung vertically on the upper shaft of an image furnace, and a piece of single crystals used as a seed rod is attached to the lower shaft. The lower end of the feed rod is heated locally to provide molten solvent intervening feed and seed rods. As the heated part is gradually shifted up, crystal growth occurs on top of the seed rod by undergoing slow cooling. Atmospheric gas can be filled in a quartz tube enclosing the crystal rods.

To obtain a high-density feed rod with a uniform composition, the sintered polycrystalline rod was once molten and solidified at a velocity of ∼20 mm/h. Using this feed rod, the single crystals were grown at a low growth velocity of ∼0.6 mm/h.

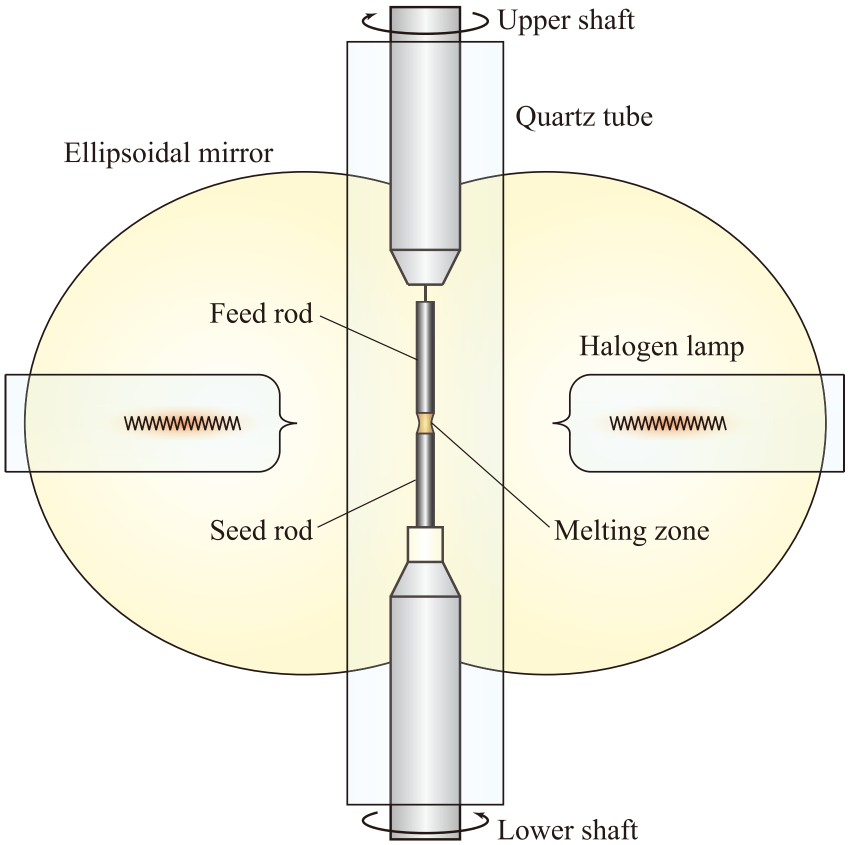


FIGURE 2.2: Schematic of the TSFZ method using an image furnace. The image furnace is equipped with two ellipsoidal mirrors, which allow a focus of the radiation emitted from the halogen lamps into the lower end of the feed rod. The heated part of the feed rod is molten to provide a melting zone between the feed and the seed rods. As the upper and lower shafts, to which the feed and seed rods are attached, is shifted downward, the melting zone is transferred upward. This leads to a crystal growth on top of the seed rod by undergoing slow cooling. The upper and lower shafts are rotated in opposite directions during the crystal growth to stir the molten solvent. The crystalline rods are enclosed by a quartz tube so that the atmospheric gas can be filled in it.

### 2.1.5 Sample Characterization

The SC critical temperature $T_c$ of $Bi_2Sr_2CaCu_2O_{8+x}$ single crystal used in the present work was determined from the diamagnetic transition curve (Fig. 2.3). The corresponding hole doping level $p$ was estimated according to the $T_c$-$p$ function reported by Groen *et al.* [89].

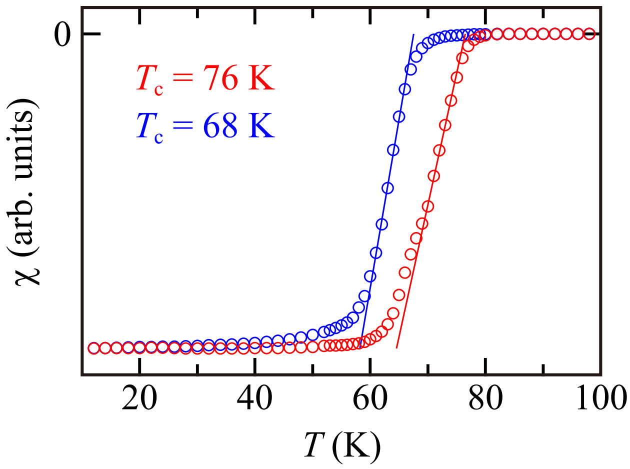


FIGURE 2.3: Temperature dependence of magnetic susceptibility measured under a magnetic field of ∼1.5 Oe for $Bi_2Sr_2CaCu_2O_{8+x}$ single crystals. STM/STS data for the samples with $T_c = 76$ K ($p \sim 0.12$) and $T_c = 68$ K ($p \sim 0.11$) are presented in Chapter 3 and Appendix G, respectively.

## 2.2 STM/STS

### 2.2.1 Basic Principles of STM

Scanning tunneling microscope (STM) [90] consists of a sharp metal tip that can be scanned across the surface of conductive sample (Fig. 2.5). When a bias voltage $V_s$ is applied to the sample with respect to the tip, a tunneling current $I$ flows through a vacuum barrier between them. This tunneling current can be measured as a function of position $\boldsymbol{r} = (x, y)$ on the sample surface.

If the sample bias voltage $V_s$ is positive, the effective Fermi level of the tip electrons shifts upwards by $eV_s$ with respect to the sample electrons, as shown in Fig. 2.4. This gives rise to the net elastic tunneling of electrons from the tip to the sample. The tunneling current from the tip to the sample

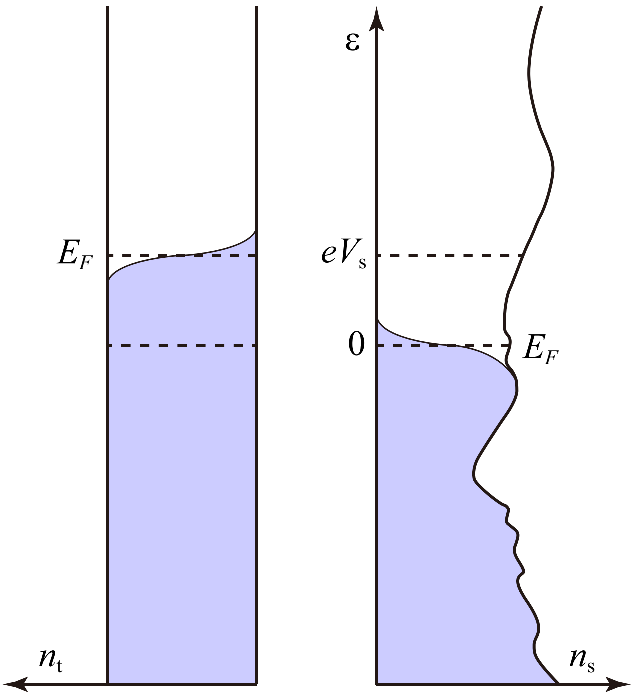


FIGURE 2.4: Schematic of tunneling from the tip (left) to the sample (right) with a positive bias voltage $V_s$ applied to the sample with respect to the tip. The regions shaded in purple indicate the filled states. The effective Fermi level of the tip electrons is shifted upwards by $eV_s$ with respect to the sample electrons. This leading to the net elastic tunneling of electrons from the tip to the sample.

is given as follows:

$$
\begin{aligned}
I =& I_{t\to s} - I_{s\to t} \\
=& -\frac{4\pi e}{\hbar}\int_{-\infty}^{\infty} |M_{ts}|^2 n_t(\varepsilon - eV_s) f(\varepsilon - eV_s) n_s(\varepsilon)[1 - f(\varepsilon)] d\varepsilon \\
& + \frac{4\pi e}{\hbar}\int_{-\infty}^{\infty} |M_{st}|^2 n_s(\varepsilon) f(\varepsilon) n_t(\varepsilon - eV_s)[1 - f(\varepsilon - eV_s)] d\varepsilon \\
=& -\frac{4\pi e}{\hbar}\int_{-\infty}^{\infty} |M|^2 n_s(\varepsilon) n_t(\varepsilon - eV_s)[f(\varepsilon - eV_s) - f(\varepsilon)] d\varepsilon.
\end{aligned}
\tag{2.1}
$$

Here, $I_{t\to s}$ and $I_{s\to t}$ denote the currents due to the elastic tunneling of electrons from the tip to the sample and vice versa, $\varepsilon$ gives the energy relative to the Fermi energy of sample electrons, $f(\varepsilon)$ is the Fermi distribution function, and $n_t(\varepsilon)$ and $n_s(\varepsilon)$ give the DOS of the tip and the sample. The tunneling matrix element $M_{ts}$ can be calculated by a surface integral over the separation space $\Sigma$ between the tip and the sample,

$$M_{\mathrm{ts}} = \frac{\hbar^2}{2m} \int_{\Sigma} (\psi_{\mathrm{t}} \boldsymbol{\nabla} \psi_{\mathrm{s}}^* - \psi_{\mathrm{s}}^* \boldsymbol{\nabla} \psi_{\mathrm{t}}) \cdot d\boldsymbol{S}, \tag{2.2}$$

where $\psi_{\mathrm{t}}$ and $\psi_{\mathrm{s}}$ are the tip and sample wave functions [91], and $|M|^2 = |M_{\mathrm{ts}}|^2 = |M_{\mathrm{st}}|^2$. Under the assumption that the tunneling matrix element $M$ and the DOS of the tip $n_{\mathrm{t}}$ are independent of energy within a range $0 < \varepsilon < eV_{\mathrm{s}}$, we have

$$I = -\frac{4\pi e}{\hbar} |M|^2 n_{\mathrm{t}} \int_0^{eV_{\mathrm{s}}} n_{\mathrm{s}}(\varepsilon) d\varepsilon \tag{2.3}$$

at $T = 0$. For an $s$-wave tip having a locally spherical geometry where it approaches nearest to the sample,

$$|M|^2 \propto |\psi_{\mathrm{s}}(\boldsymbol{R}_0)|^2 \propto e^{-2\kappa z} |\psi_{\mathrm{s}}(x, y, z = 0)|^2, \tag{2.4}$$

where $\boldsymbol{R}_0 = (x, y, z = Z_0)$ gives the position of the center of curvature of the tip, $z$ is the tip-sample distance, and

$$\kappa = \frac{\sqrt{2m\phi}}{\hbar} \tag{2.5}$$

with $\phi$ being the work function is the inverse decay length of wave functions in vacuum [92, 93]. The decay length $\kappa^{-1}$ is of the order of $\sim$1 Å for the typical values of work function $\sim$5 eV [94]. This exponential dependence on the tip height $z$ is what making the tunneling current measured by STM sensitive to the surface topography.

The discussion above leads to the tunneling current of the form

$$I(\boldsymbol{r}, z, V_{\mathrm{s}}) = C \exp(-2\kappa z) \int_0^{eV_{\mathrm{s}}} n_{\mathrm{s}}(\boldsymbol{r}, \varepsilon) d\varepsilon, \tag{2.6}$$

where $C$ is a proportional constant, and

$$n_{\mathrm{s}}(\boldsymbol{r}, \varepsilon) = n_{\mathrm{s}}(\varepsilon) |\psi_{\mathrm{s}}(\boldsymbol{r}, z = 0)|^2 \tag{2.7}$$

is the LDOS of the sample at a position $\boldsymbol{r} = (x, y)$. The tunneling current $I(\boldsymbol{r}, z, V_{\mathrm{s}})$ is proportional to the energy-integrated LDOS of the sample at a given position.

### 2.2.2 Modes of Operation

When scanning the tip across the sample surface, there are two different modes of operation: constant-current and constant-height modes.

In constant-current mode, the tip height $z$ is adjusted by a feedback loop as the tip scans across the sample surface so that the tunneling current given by Eq. 2.6 is kept constant at a setup current $I_{\mathrm{set}}$ under a given setup bias voltage $V_{\mathrm{set}}$. The tip height

$$z(\boldsymbol{r}, I_{\mathrm{set}}, V_{\mathrm{set}}) = \frac{1}{2\kappa} \ln \left[ \frac{C}{I_{\mathrm{set}}} \int_0^{eV_{\mathrm{set}}} n_{\mathrm{s}}(\boldsymbol{r}, \varepsilon) d\varepsilon \right] \tag{2.8}$$

is then recorded as a function of position $\boldsymbol{r}$ to provide a topographic image.

On the other hand, in constant-height mode, the tip height $z$ is kept constant at $z = z_0$ as the tip scans across the sample surface, and the tunneling current under a given setup bias voltage $V_{\mathrm{set}}$,

$$I(\boldsymbol{r}, z_0, V_{\mathrm{set}}) = C \exp(-2\kappa z_0) \int_0^{eV_{\mathrm{set}}} n_{\mathrm{s}}(\boldsymbol{r}, \varepsilon) d\varepsilon \tag{2.9}$$

is recorded as a function of position $\boldsymbol{r}$ to provide a current image.

### 2.2.3 Constant-current $dI/dV$ Imaging

By differentiating Eq. 2.6 with respect to $V_{\mathrm{s}}$, we have

$$G(\boldsymbol{r}, z, V_{\mathrm{s}}) \equiv \frac{\partial I(\boldsymbol{r}, z, V_{\mathrm{s}})}{\partial V_{\mathrm{s}}} = C \exp(-2\kappa z) e n_{\mathrm{s}}(\boldsymbol{r}, E = eV_{\mathrm{s}}). \tag{2.10}$$

The differential conductance $dI/dV$ is proportional to the LDOS at a given energy $E = eV_{\mathrm{s}}$. This allows the atomically resolved spectroscopic measurement with the use of STM, called STS.

In order to measure a $dI/dV$ spectrum, or $G(\boldsymbol{r}, z, V_{\mathrm{s}})$ as a function of $V_{\mathrm{s}}$, the bias voltage is swept while holding the tip height $z$ and position $\boldsymbol{r}$. Then, a small AC modulation from a lock-in amplifier is superimposed on the sweep bias voltage $V_{\mathrm{s}}$,

$$V(t) = V_{\mathrm{s}} + V_{\mathrm{m}} \cos(\omega t + \phi). \tag{2.11}$$

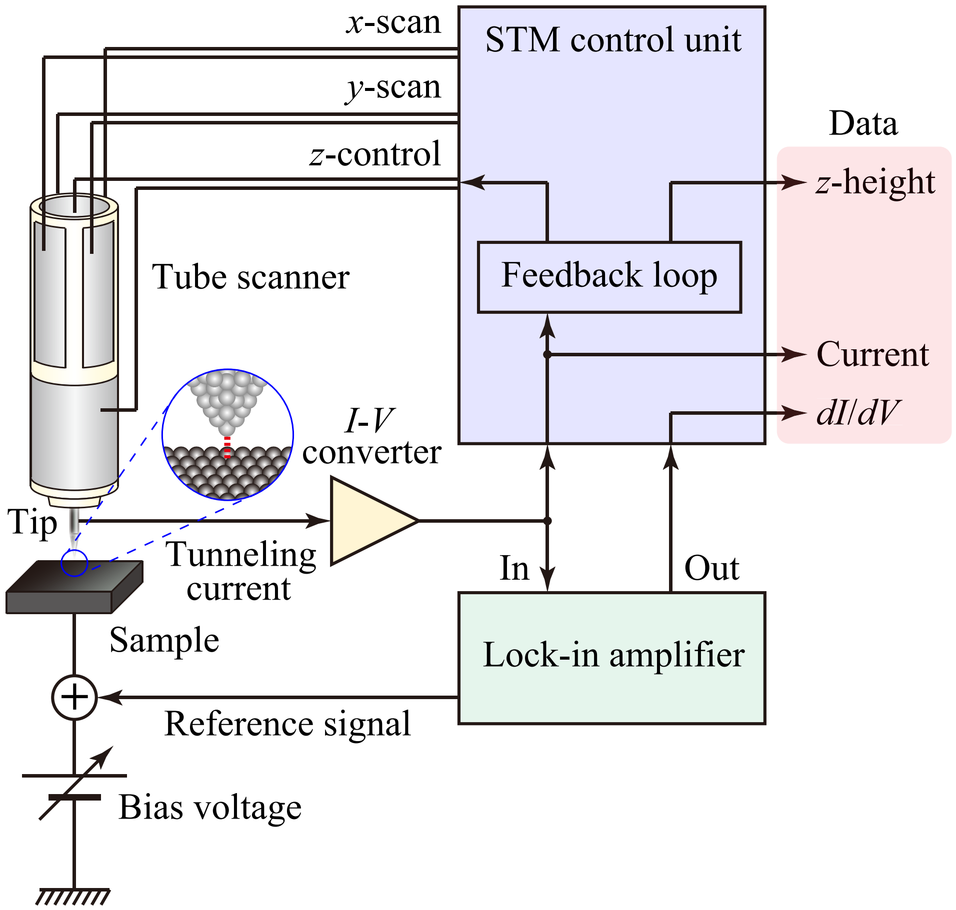


FIGURE 2.5: Schematic of STM operation. The tunneling current flowing through a vacuum barrier between the tip and the voltage-biased sample is measured. The tip is attached to a piezoelectric tube scanner to adjust the tip height $z$ using a feedback system, as well as to scan the tip in the $x$ and $y$ directions. In constant-current mode, the tip height $z$ is controlled by a feedback loop to give a constant tunneling current. A lock-in amplifier is used in spectroscopies measuring the differential conductance $dI/dV$. In spectroscopies, a small AC signal is superimposed on the bias voltage $V_\mathrm{s}$, and the differential conductance $dI/dV$ is measured through the resulting AC modulation in the tunneling current.

This gives rise to a modulation in the tunneling current,

$$\begin{aligned} I(\boldsymbol{r}, z, V(t)) =& I(r, z, V_\mathrm{s}) + \left.\frac{\partial I(\boldsymbol{r}, z, V)}{\partial V}\right|_{V_\mathrm{s}} V_\mathrm{m} \cos(\omega t + \phi) \\ &+ \frac{1}{2} \left.\frac{\partial^2 I(\boldsymbol{r}, z, V)}{\partial V^2}\right|_{V_\mathrm{s}} V_\mathrm{m}^2 \cos^2(\omega t + \phi) + \cdots . \end{aligned} \tag{2.12}$$

The differential conductance $G(\boldsymbol{r}, z, V_\mathrm{s})$ can be known from the magnitude of first harmonic measured by using the lock-in amplifier.

The $dI/dV$ spectra can be collected systematically on a two-dimensional dense array of measurement points on the sample surface. This allows constructing spatial maps of $dI/dV$ values at given bias voltages, or $G(\boldsymbol{r}, V_{\mathrm{s}})$ maps. In this method, the tip height $z$ is set at each measurement point on the sample surface to attain a constant setup current $I_{\mathrm{set}}$ under a setup bias voltage $V_{\mathrm{set}}$. The $dI/dV$ spectrum for the corresponding measurement point is then measured while the tip height $z$ is sustained by turning off the feedback loop. After collecting every spectrum, $dI/dV$ values for a specified bias voltage are mapped to obtain a $G_{\mathrm{cc}}(\boldsymbol{r}, V_{\mathrm{s}})$ map.

### 2.2.4 The Setup Effect and Setup-free Function

The constant-current setting of tip height described above can lead to a spatially varying tip height as in Eq. 2.8. Since the differential conductance given by Eq. 2.10 reflects the tip height through the factor $e^{-2\kappa z}$, this spatial variation in $z$ can affect the resultant $G_{\mathrm{cc}}(\boldsymbol{r}, V_{\mathrm{s}})$ maps. Substituting Eq. 2.8 into Eq. 2.10, this becomes

$$G_{\mathrm{cc}}(\boldsymbol{r}, V_{\mathrm{s}}, V_{\mathrm{set}}, I_{\mathrm{set}}) = \frac{eI_{\mathrm{set}} n_{\mathrm{s}}(\boldsymbol{r}, E = eV_{\mathrm{s}})}{\int_0^{eV_{\mathrm{set}}} n_{\mathrm{s}}(\boldsymbol{r}, \varepsilon) d\varepsilon}. \tag{2.13}$$

Equation 2.13 indicates that the conductance modulations included in the integral of the LDOS over the range of energies 0 to $eV_{\mathrm{set}}$ appear in the resultant $G_{\mathrm{cc}}(\boldsymbol{r}, V_{\mathrm{s}})$ maps for all energies. This effect giving rise to a reflection of conductance modulation from a set of energy region to another is called the setup effect [26, 38].

Obviously, the setup effect comes from the energy-integrated LDOS in the denominator of Eq. 2.13. As $G_{\mathrm{cc}}(\boldsymbol{r}, V_{\mathrm{s}})$ for all $V_{\mathrm{s}}$ have this factor in common, one can eliminate the possible setup effect by constructing a map of ratio of $G_{\mathrm{cc}}(\boldsymbol{r}, V_{\mathrm{s}})$ values for two bias voltages with the same amplitude and opposite polarity [26, 27]:

$$Z_{\mathrm{cc}}(\boldsymbol{r}, V_{\mathrm{s}}) \equiv \frac{G_{\mathrm{cc}}(\boldsymbol{r}, +V_{\mathrm{s}}, V_{\mathrm{set}}, I_{\mathrm{set}})}{G_{\mathrm{cc}}(\boldsymbol{r}, -V_{\mathrm{s}}, V_{\mathrm{set}}, I_{\mathrm{set}})} = \frac{n_{\mathrm{s}}(\boldsymbol{r}, E = +eV_{\mathrm{s}})}{n_{\mathrm{s}}(\boldsymbol{r}, E = -eV_{\mathrm{s}})}. \tag{2.14}$$

On the other hand, taking such a ratio results in a mixture of conductance modulations at different bias voltages $\pm V_{\mathrm{s}}$. Nevertheless, the $Z_{\mathrm{cc}}(\boldsymbol{r}, V_{\mathrm{s}})$ map is still convenient to investigate the QPI modulation, whose spatial phase is reversed with the inversion of bias polarity [30]. With the use of $Z_{\rm cc}(\boldsymbol{r}, V_{\rm s})$ map, QPI modulation can be separated from the CB modulation [26] since the CB modulation, whose amplitude and phase are independent of bias polarity [43, 55], is weakened in the $Z_{\rm cc}(\boldsymbol{r}, V_{\rm s})$ map, whereas the QPI modulation remains.

Based on this observation, however, it has been suggested that the CB modulation observed in the low-energy LDOS may be an extrinsic modulation due to the setup effect [26]. Thus, for a careful investigation of the CB modulation, it is to be desired that the low-energy LDOS is measured by a method free from the setup effect.

### 2.2.5 Constant-height $dI/dV$ Imaging

As presented in Section 2.2.4, the setup effect arises from the spatial variation of the tip height. Therefore, if a $G(\boldsymbol{r}, V_{\rm s})$ map is measured in constant-height mode, it will be free from the setup effect [95]. This method of $dI/dV$ imaging, together with the low-bias STM imaging [96, 97], has been developed in our group [55].

In constant-height $dI/dV$ imaging, a small AC modulation from a lock-in amplifier is superimposed on the DC bias voltage $V_{\rm s}$ while taking a current image in constant-height mode,

$$V(t) = V_{\rm s} + V_{\rm m}\cos(\omega t + \phi). \tag{2.15}$$

The tunneling current is then given by

$$\begin{aligned} I(\boldsymbol{r}, z_0, V(t)) =& I(r, z_0, V_{\rm s}) + \left.\frac{\partial I(\boldsymbol{r}, z_0, V)}{\partial V}\right|_{V_{\rm s}} V_{\rm m}\cos(\omega t + \phi) \\ &+ \frac{1}{2}\left.\frac{\partial^2 I(\boldsymbol{r}, z_0, V)}{\partial V^2}\right|_{V_{\rm s}} V_{\rm m}^2\cos^2(\omega t + \phi) + \cdots \end{aligned} \tag{2.16}$$

where $z_0$ is the constant tip height. The magnitude of the first harmonic

$$G_{\rm ch}(\boldsymbol{r}, z_0, V_{\rm s}) \equiv \frac{\partial I(\boldsymbol{r}, z_0, V_{\rm s})}{\partial V_{\rm s}} = C\exp(-2\kappa z_0) e n_{\rm s}(\boldsymbol{r}, E = eV_{\rm s}) \tag{2.17}$$

measured by the lock-in amplifier is directly imaged to gain a $G_{\mathrm{ch}}(\boldsymbol{r}, z_0, V_{\mathrm{s}})$ map. Essentially, a $G_{\mathrm{ch}}(\boldsymbol{r}, z_0, V_{\mathrm{s}})$ map measured at $V_{\mathrm{s}}$ does not contain any conductance modulations at bias voltages out of the range $V_{\mathrm{s}} \pm V_{\mathrm{m}}$.

The tip height $z_0$, which is constant in a $G_{\mathrm{ch}}(\boldsymbol{r}, z_0, V_{\mathrm{s}})$ map, is determined by the feedback system so that the tunneling current given by Eq. 2.9 has a value equal to the setup current $I_{\mathrm{set}}$ under the bias voltage $V_{\mathrm{s}}$ at a specified position $\boldsymbol{r} = \boldsymbol{r}_0$,

$$z_0(\boldsymbol{r}_0, V_{\mathrm{s}}, I_{\mathrm{set}}) = \frac{1}{2\kappa} \ln \left[ \frac{C}{I_{\mathrm{set}}} \int_0^{eV_{\mathrm{s}}} n_{\mathrm{s}}(\boldsymbol{r}_0, \varepsilon) d\varepsilon \right]. \tag{2.18}$$

Therefore, when two $G_{\mathrm{ch}}(\boldsymbol{r}, z_0, V_{\mathrm{s}})$ maps are measured in the same field of view, the different choice of $V_{\mathrm{s}}$ generally results in different values of $z_0$ between them. Obviously, this will affect the relative amplitude of conductance modulations in these $G_{\mathrm{ch}}(\boldsymbol{r}, z_0, V_{\mathrm{s}})$ maps, through the factor $e^{-2\kappa z_0}$ in Eq. 2.17. Substituting Eq. 2.18 into Eq. 2.17 yields

$$G_{\mathrm{ch}}(\boldsymbol{r}, V_{\mathrm{s}}, I_{\mathrm{set}}) = \frac{eI_{\mathrm{set}} n_{\mathrm{s}}(\boldsymbol{r}, E = eV_{\mathrm{s}})}{\int_0^{eV_{\mathrm{s}}} n_{\mathrm{s}}(\boldsymbol{r}_0, \varepsilon) d\varepsilon}, \tag{2.19}$$

indicating that the amplification factor $eI_{\mathrm{set}} / \int_0^{eV_{\mathrm{s}}} n_{\mathrm{s}}(\boldsymbol{r}_0, \varepsilon) d\varepsilon$ depends on $V_{\mathrm{s}}$ and $I_{\mathrm{set}}$.

Fortunately, in the SC state of $Bi_2Sr_2CaCu_2O_{8+x}$, $dI/dV$ spectra are almost particle-hole symmetric in the low-energy region where CB and QPI modulations live (see Appendix A), leading to

$$\int_{-eV_{\mathrm{s}}}^{0} n_{\mathrm{s}}(\boldsymbol{r}, \varepsilon) d\varepsilon \simeq \int_0^{+eV_{\mathrm{s}}} n_{\mathrm{s}}(\boldsymbol{r}, \varepsilon) d\varepsilon. \tag{2.20}$$

Thus, measuring $G_{\mathrm{ch}}(\boldsymbol{r}, \pm V_{\mathrm{s}}, I_{\mathrm{set}})$ maps for the same field of view under a setup current $I_{\mathrm{set}}$ with the same amplitude equates the values of amplification factors $eI_{\mathrm{set}} / \int_0^{eV_{\mathrm{s}}} n_{\mathrm{s}}(\boldsymbol{r}_0, \varepsilon) d\varepsilon$, allowing a comparison of modulation amplitude within these $G_{\mathrm{ch}}(\boldsymbol{r}, \pm V_{\mathrm{s}}, I_{\mathrm{set}})$ maps. Moreover, this justifies the definition of $Z_{\mathrm{ch}}(\boldsymbol{r}, V_{\mathrm{s}})$ map that is essentially equivalent to the $Z_{\mathrm{cc}}(\boldsymbol{r}, V_{\mathrm{s}})$ map:

$$Z_{\mathrm{ch}}(\boldsymbol{r}, V_{\mathrm{s}}) \equiv \frac{G_{\mathrm{ch}}(\boldsymbol{r}, +V_{\mathrm{s}}, I_{\mathrm{set}})}{G_{\mathrm{ch}}(\boldsymbol{r}, -V_{\mathrm{s}}, I_{\mathrm{set}})} = \frac{n_{\mathrm{s}}(\boldsymbol{r}, E = +eV_{\mathrm{s}})}{n_{\mathrm{s}}(\boldsymbol{r}, E = -eV_{\mathrm{s}})}. \tag{2.21}$$

In the present study, each pair of low-bias $G_{\mathrm{ch}}(\boldsymbol{r}, \pm V_{\mathrm{s}})$ maps were measured to satisfy the requirement above. This allows the evaluation of modulation amplitude within each pair of $G_{\mathrm{ch}}(\boldsymbol{r}, \pm V_{\mathrm{s}})$ maps, and within their $Z_{\mathrm{ch}}(\boldsymbol{r}, V_{\mathrm{s}})$ maps. More importantly, this provides a foundation for the separation of the CB and QPI modulations presented in Section 3.1.

# Chapter 3

# Spatial Relationship between CB and QPI Modulations

To investigate the spatial relationship between CB and QPI modulations, constant-height $dI/dV$ imaging was performed in the SC state ($T = 7$ K) of underdoped $Bi_2Sr_2CaCu_2O_{8+x}$ ($p \sim 0.12$ and $T_c = 76$ K). The $G(\boldsymbol{r}, V_s)$ maps were measured at low bias voltages of $V_s = \pm 30$, $\pm 20$, and $\pm 10$ mV in the same field of view where atomically resolved topography shown in Fig. 3.1 was measured. The values of applied bias voltages correspond to energies smaller than the $d$-wave SC gap amplitude $\Delta_0 \sim 40$ meV for this hole-doping level [97, 98]. As shown in the inset of Fig. 3.2, $dI/dV$ spectra measured in the cleaved surface exhibit sub gaps at $|V_s| \sim \pm 25$ mV$(= \Delta_{SG}/e)$ in addition to the spatially inhomogeneous pseudogap at larger energy scale $\Delta_{PG}$ (see Appendix A for details of $dI/dV$ spectra).

## 3.1 Coexistence of CB and QPI Modulations

### 3.1.1 Electronic Superstructure in Low-energy LDOS

Figures 3.2(a) and 3.2(c) show $G(\boldsymbol{r}, V_s)$ maps for $V_s = +20$ and $-20$ mV, with the corresponding Fourier transform (FT) maps $|\tilde{G}(\boldsymbol{q}, V_s)|$ shown in Fig. 3.2(b) and 3.2(d). The data for other bias voltages can be found in Appendix B. In $G(\boldsymbol{r}, V_s)$ maps, one can see a checkerboardlike electronic superstructure along the two orthogonal Cu-O bond directions, yielding broad Fourier spots (solid red circles) on the $q_x$ and $q_y$ axes that extend from the origin towards the Bragg spots (dashed black circles).

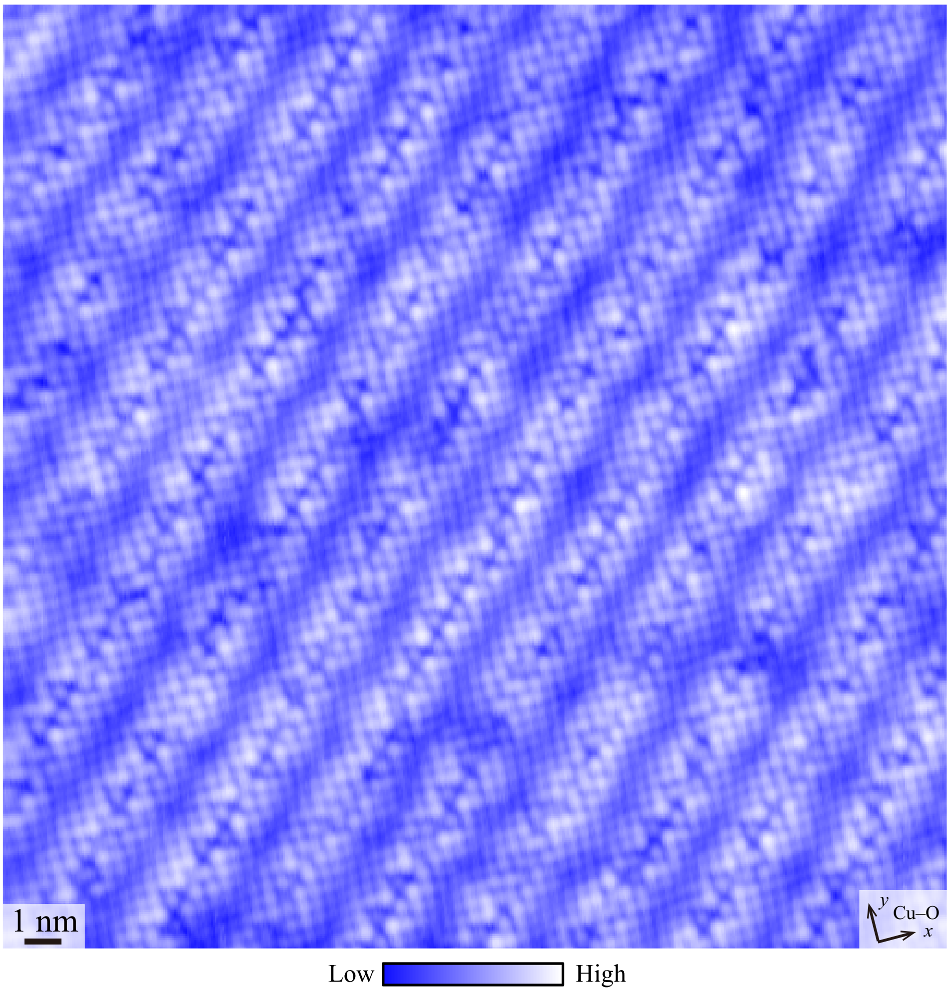


FIGURE 3.1: Atomically resolved topography of the underdoped $Bi_2Sr_2CaCu_2O_{8+x}$ ($p \sim 0.12$ and $T_c = 76$ K) for $V_s = +100$ mV measured at 7 K. The $x$ and $y$ axes (arrows) indicates the Cu-O bond directions. One-dimensional structural superlattice of BiO plane runs along the $b$ axis inclined 45° to the Cu-O bond directions.

Figure 3.2(e) shows line cuts of the FT maps $|\tilde{G}(\boldsymbol{q}, V_s)|$ along the $q_y$ axis plotted in a scale as $2\pi/a = 1$ ($a$: Cu-O-Cu distance). The Fourier peaks of the electronic superstructure are roughly estimated to be centered around $q_y = 1/4$ for all bias voltages studied, being reminiscent of the nondispersive CB modulation. However, they seem to contradict the nature of CB modulation that its amplitude and phase do not change with the sign change of bias voltage [43, 55]. In the present case, the intensity at $q_y \sim 1/4$ is larger at positive bias voltages $+V_s$ than negative ones $-V_s$, especially for $V_s = 20$ and 30 mV.

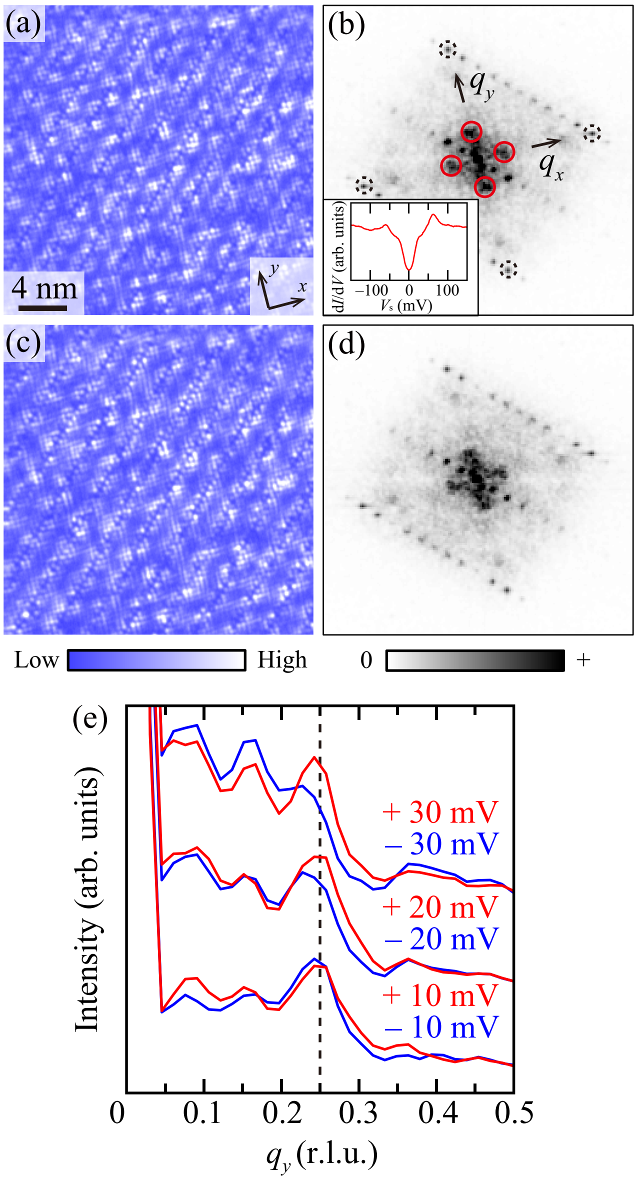


FIGURE 3.2: $G(\boldsymbol{r}, V_s)$ maps: (a) for $V_s = +20$ mV and (c) for $V_s = -20$ mV. A checkerboardlike electronic superstructure along the two Cu-O bond directions is observed. The one-dimensional structural superlattice of the BiO plane is also confirmed seemingly due to the indirect tunneling between the tip and the $CuO_2$ plane that involves intermediate states consisting of $6p_z$ of Bi and $4s$ or $3d_{3z^2-r^2}$ of Cu [55,99]. FT maps $|\tilde{G}(\boldsymbol{q}, V_s)|$: (b) for $V_s = +20$ mV and (d) for $V_s = -20$ mV. Solid and dashed circles indicate the Fourier spots corresponding to the electronic superstructure and the Bragg spots, respectively. The inset shows a typical example of $dI/dV$ spectra measured in the same cleaved surface. It exhibits sub gaps at $V_s \sim \pm 25$ mV within the spatially inhomogeneous pseudogap at larger energies. (e) Line cuts of the FT maps $|\tilde{G}(\boldsymbol{q}, V_s)|$ on the $q_y$ axis plotted in a reciprocal lattice unit (r.l.u.) defined as $2\pi/a = 1$ for $V_s = \pm 10$, $\pm 20$, and $\pm 30$ mV.

Thus far, a similar behavior has been confirmed by constant-current $dI/dV$ imaging [52, 53, 82], remaining a possibility that the asymmetric intensity at CB wave vector could be associated with the setup effect [26, 38, 52]. However, the present results of constant-height $dI/dV$ imaging, which is substantially free from the setup effect [95], clearly demonstrate that the observed asymmetry in the intensity at $q_y \sim 1/4$ is intrinsic to the electronic superstructure. One may infer from the present data that the CB modulation itself might be asymmetric for the inversion of bias polarity; i.e., the low-energy states in the antinodal region might exhibit electron-hole asymmetry [53]. However, it has been pointed out that the QPI modulation, whose $\boldsymbol{q}_1$ component has a wave vector similar to that of CB modulation, is also observed in low-bias $G(\boldsymbol{r}, V_\mathrm{s})$ maps [26, 51], implying that the Fourier signal at $q_y \sim 1/4$ contains not only CB but also $\boldsymbol{q}_1$-QPI signatures. Thus, for understanding the origin of asymmetric intensity at $q_y \sim 1/4$, as well as for investigating the spatial relationship between CB and QPI modulations, these two superstructures have to be disentangled first.

### 3.1.2 Separation of QPI Modulation

It is well established that QPI modulation can be extracted by constructing a map of the ratios of $G(\boldsymbol{r}, \pm V_\mathrm{s})$ values at bias voltages of the opposite sign [26, 27, 30],

$$Z(\boldsymbol{r}, V_\mathrm{s}) \equiv \frac{G(\boldsymbol{r}, +V_\mathrm{s})}{G(\boldsymbol{r}, -V_\mathrm{s})}. \tag{3.1}$$

Generally, the spatial modulation at finite wave vector $\boldsymbol{q}$ in $G(\boldsymbol{r}, V_\mathrm{s})$ map $G_{\boldsymbol{q}}(\boldsymbol{r}, V_\mathrm{s})$ is substantially smaller than the uniform background $G_0(V_\mathrm{s})$,

$$\frac{G_{\boldsymbol{q}}(\boldsymbol{r}, V_\mathrm{s})}{G_0(V_\mathrm{s})} \ll 1. \tag{3.2}$$

Then, $Z(\boldsymbol{r}, V_\mathrm{s})$ is given as follows:

$$\begin{aligned} Z(\boldsymbol{r}, V_\mathrm{s}) &= \frac{G_0(+V_\mathrm{s}) + \sum_{\boldsymbol{q}} G_{\boldsymbol{q}}(\boldsymbol{r}, +V_\mathrm{s})}{G_0(-V_\mathrm{s}) + \sum_{\boldsymbol{q}} G_{\boldsymbol{q}}(\boldsymbol{r}, -V_\mathrm{s})} \\ &\sim \frac{G_0(+V_\mathrm{s})}{G_0(-V_\mathrm{s})} \left[1 + \frac{\sum_{\boldsymbol{q}} G_{\boldsymbol{q}}(\boldsymbol{r}, +V_\mathrm{s})}{G_0(+V_\mathrm{s})} + \frac{\sum_{\boldsymbol{q}} G_{\boldsymbol{q}}(\boldsymbol{r}, -V_\mathrm{s})}{G_0(-V_\mathrm{s})}\right]. \end{aligned} \tag{3.3}$$

As presented in Appendix A, $G_0(V_\mathrm{s})$ is almost independent of bias polarity,

$$G_0(+V_\mathrm{s}) = G_0(-V_\mathrm{s}), \tag{3.4}$$

at least for small bias voltages $|V_\mathrm{s}| \leq 30$ mV studied, leading to

$$Z(\boldsymbol{r}, V_\mathrm{s}) \sim 1 + \frac{1}{G_0(V_\mathrm{s})} \sum_{\boldsymbol{q}} \left[G_{\boldsymbol{q}}(\boldsymbol{r}, +V_\mathrm{s}) - G_{\boldsymbol{q}}(\boldsymbol{r}, -V_\mathrm{s})\right]. \tag{3.5}$$

This expression indicates that the spatial modulation at $\boldsymbol{q}$ in $Z(\boldsymbol{r}, V_\mathrm{s})$ map is proportional to that in a map defined as $G_{\boldsymbol{q}}(\boldsymbol{r}, +V_\mathrm{s}) - G_{\boldsymbol{q}}(\boldsymbol{r}, -V_\mathrm{s})$. Therefore, the CB modulation, whose amplitude and phase are almost independent of bias polarity [43, 55] is weakened in $Z(\boldsymbol{r}, V_\mathrm{s})$ map. On the other hand, QPI modulation, whose phases have been considered to be reversed with the inversion of bias polarity [30], remains in $Z(\boldsymbol{r}, V_\mathrm{s})$ map [26, 27].

Figures 3.3(a) and 3.3(b) show the $Z(\boldsymbol{r}, V_\mathrm{s})$ map and the corresponding FT map $|\tilde{Z}(\boldsymbol{q}, V_\mathrm{s})|$ for $V_\mathrm{s} = +20$ mV, respectively (see Appendix C for the data at other bias voltages). In the FT map, we can identify seven kinds of spots, marked $\boldsymbol{q}_1$–$\boldsymbol{q}_7$, corresponding to the seven independent components of QPI modulation. Line cuts of the FT maps $|\tilde{Z}(\boldsymbol{q}, V_\mathrm{s})|$ along the $q_y$ axis are shown in Fig. 3.3(c). The Fourier peaks corresponding to the $\boldsymbol{q}_1$ component are confirmed near $q_y \sim 1/4$. For each bias voltage, the wave vector $\boldsymbol{q}_{1y}$ of $\boldsymbol{q}_1$-QPI along the $q_y$ axis was determined by the demodulation phase residue minimization technique [35], and the corresponding wave number $|\boldsymbol{q}_{1y}|$ is indicated by a bar on top of the line cuts (see Appendix E for the determination of the wave vector). The wave number $|\boldsymbol{q}_{1y}|$ is closest to that of nondispersive CB modulation at $|V_\mathrm{s}| = 30$ mV and becomes larger away from it with decreasing $|V_\mathrm{s}|$. This weakly dispersive behavior indicates that the QPI modulation including $\boldsymbol{q}_1$ component is reasonably extracted from the low-energy $G(\boldsymbol{r}, V_\mathrm{s})$ maps.

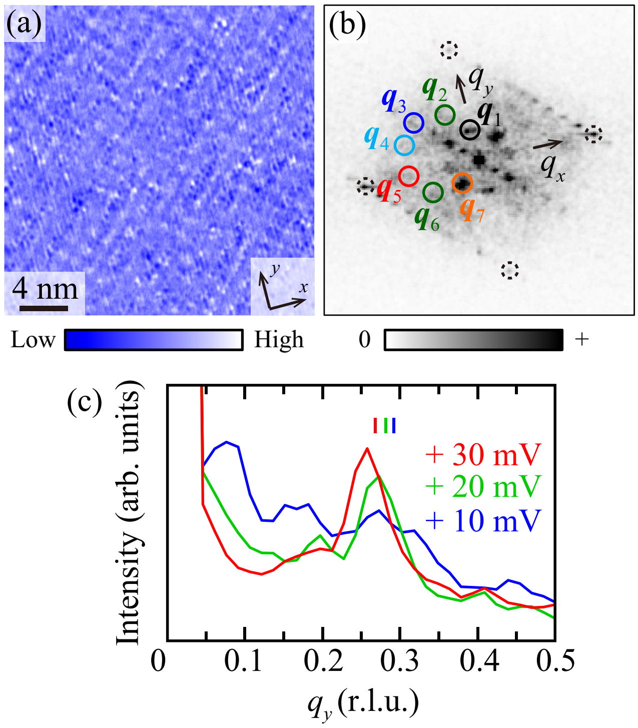


FIGURE 3.3: (a) $Z(\boldsymbol{r}, V_\mathrm{s})$ map for $V_\mathrm{s} = +20$ mV. (b) FT map $|\tilde{Z}(\boldsymbol{q}, V_\mathrm{s})|$ for $V_\mathrm{s} = +20$ mV. Solid circles indicate the Fourier spots corresponding to the seven independent components of QPI, $\boldsymbol{q}_1$–$\boldsymbol{q}_7$. (c) Line cuts of FT maps $|\tilde{Z}(\boldsymbol{q}, V_\mathrm{s})|$ on the $q_y$ axis for $V_\mathrm{s} = +10$, $+20$, and $+30$ mV. The position of each small bar indicates the wave number of weakly dispersive $\boldsymbol{q}_1$-QPI modulation $|\boldsymbol{q}_{1y}|$ determined by the demodulation phase residue minimization technique. For $V_\mathrm{s} = +10$ mV, the demodulation phase residue exhibits two independent minima, corresponding to two separated peaks near $q_y \sim 0.29$ in the line cut, and thus their mean wave vector was adopted as $\boldsymbol{q}_{1y}$.

### 3.1.3 Separation of CB Modulation

To separate the CB modulation from the QPI modulation, I introduce an $S(\boldsymbol{r}, |V_\mathrm{s}|)$ map defined as the following equation:

$$S(\boldsymbol{r}, |V_\mathrm{s}|) \equiv \frac{G(\boldsymbol{r}, +V_\mathrm{s}) + G(\boldsymbol{r}, -V_\mathrm{s})}{2}. \tag{3.6}$$

By definition, the $S(\boldsymbol{r}, |V_\mathrm{s}|)$ map gives the symmetric component in $G(\boldsymbol{r}, \pm V_\mathrm{s})$ maps. This will result in a suppression of QPI modulation if it is antisymmetric with respect to the inversion of bias polarity, leaving CB modulation of being almost symmetric.

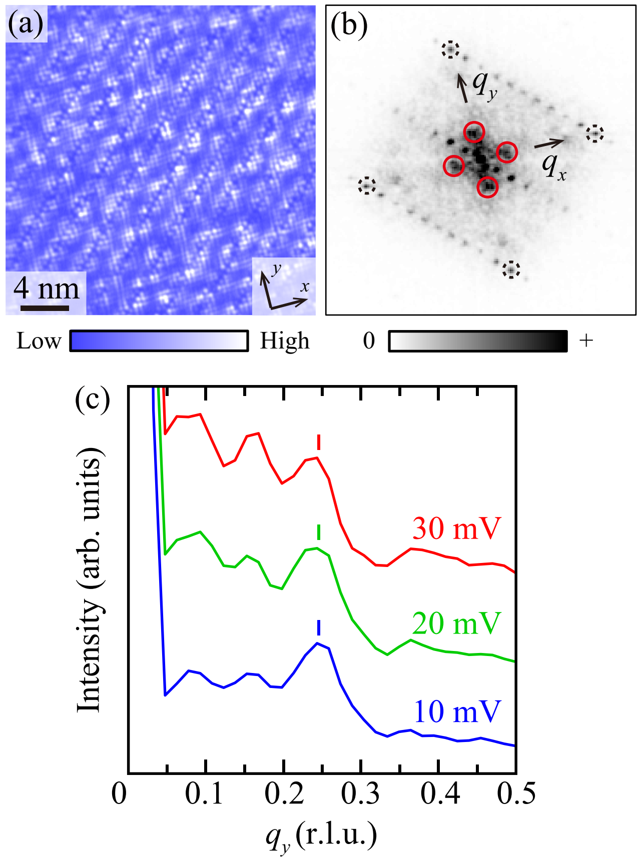


FIGURE 3.4: (a) $S(\boldsymbol{r}, |V_s|)$ map for $|V_s| = 20$mV. (b) FT map $|\tilde{S}(\boldsymbol{q}, |V_s|)|$ for $|V_s| = 20$mV. Solid and dashed circles indicate the Fourier spots of CB modulation and the Bragg spots, respectively. (c) Line cuts of FT maps $|\tilde{S}(\boldsymbol{q}, |V_s|)|$ on the $q_y$ axis for $V_s = +10$, $+20$, and $+30$ mV. The position of each small bar indicates the wave number of CB modulation $|\boldsymbol{Q}_y|$ determined by the demodulation phase residue minimization technique.

Figures 3.4(a) and 3.4(b) show the $S(\boldsymbol{r}, |V_s|)$ map and the corresponding FT map $|\tilde{S}(\boldsymbol{q}, |V_s|)|$ for $|V_s| = 20$ mV (see Appendix D for the data at other bias voltages). As expected, a checkerboardlike pattern similar to that in $G(\boldsymbol{r}, \pm V_s)$ maps is confirmed in the $S(\boldsymbol{r}, |V_s|)$ map, yielding Fourier spots at similar wave vectors. In line cuts of FT maps $|\tilde{S}(\boldsymbol{q}, |V_s|)|$ along the $q_y$ axis [Fig. 3.4(c)], one can see the corresponding Fourier peak at $q_y \sim 1/4$, whose central position seems to be unchanged for the bias voltages examined. Indeed, its wave vector $\boldsymbol{Q}_y$ determined by the demodulation phase residue minimization technique [35] are totally independent of bias voltage (see Appendix E for the determination of the wave vector), resulting in a constant wave number $|\boldsymbol{Q}_y|$ indicated by bars on top of the line cuts. This nondispersive behavior demonstrates that the CB modulation was successfully separated from the QPI modulation.

Finally, by comparing $G(\boldsymbol{r}, V_\mathrm{s})$ and $S(\boldsymbol{r}, |V_\mathrm{s}|)$ maps, one can obviously see that the spatial pattern does not change largely before or after the subtraction of QPI modulation. This is indicative of a predominance of the CB modulation over the QPI modulation in intensity. Nevertheless, the separation of CB and QPI modulations presented above firmly establishes their coexistence in identical regions of the $\mathrm{CuO_2}$ plane, supporting their symmetric and antisymmetric natures with respect to the sign change of bias voltage.

## 3.2 Local Properties of CB and $\boldsymbol{q}_1$-QPI Modulations

The satisfactory separation of CB and QPI modulations presented in Section 3.1 leads us to the investigation on the local properties of each superstructure by itself. In this section, CB and $\boldsymbol{q}_1$-QPI modulations along the $y$ direction, which are characterized by similar wave vectors, will be extracted to evaluate their local amplitudes and phases [34].

### 3.2.1 Local Amplitude and Phase of CB Modulation

The CB modulation along the $y$ direction is given by an inverse FT of the complex-valued FT signals $\tilde{S}(\boldsymbol{q}, |V_\mathrm{s}|)$ surrounding $\boldsymbol{q} = \boldsymbol{Q}_y$. These FT signals can be cut out by multiplying a radial Gaussian-type mask function $e^{-(\boldsymbol{q}-\boldsymbol{Q}_y)^2/2\Lambda^2}$ for $|\boldsymbol{q} - \boldsymbol{Q}_y| \leq \sqrt{2\ln 2}\Lambda$ (half width at half maximum) $\sim 0.05$ and otherwise 0. Here, $\Lambda^{-1}$ gives a course graining length scale below which the filtered real-space signals cannot be resolved. The inverse FT provides a real-valued two-dimensional signal that contains modulations at wave vectors proximal to $\boldsymbol{Q}$ in the $S(\boldsymbol{r}, |V_\mathrm{s}|)$ map. This filtered signal can be extended to a complex-valued analytic signal $\tilde{S}_{\boldsymbol{Q}_y}(\boldsymbol{r}, |V_\mathrm{s}|)$, whose real and imaginary parts are given by the filtered signal itself and that delayed by $\pi/2$, respectively (see Appendix F for the calculated analytic signals). Then, the local amplitude is given by the magnitude of $\tilde{S}_{\boldsymbol{Q}_y}(\boldsymbol{r}, |V_\mathrm{s}|)$,

$$A^S_{\boldsymbol{Q}_y}(\boldsymbol{r}, |V_\mathrm{s}|) = \sqrt{\left[\mathrm{Re}\tilde{S}_{\boldsymbol{Q}_y}(\boldsymbol{r}, |V_\mathrm{s}|)\right]^2 + \left[\mathrm{Im}\tilde{S}_{\boldsymbol{Q}_y}(\boldsymbol{r}, |V_\mathrm{s}|)\right]^2}, \tag{3.7}$$

while the local phase is given by the argument of $\tilde{S}_{\boldsymbol{Q}_y}(\boldsymbol{r}, |V_\mathrm{s}|)$,

$$\varphi^S_{\boldsymbol{Q}_y}(\boldsymbol{r}, |V_\mathrm{s}|) = \arctan\left[\frac{\mathrm{Im}\tilde{S}_{\boldsymbol{Q}_y}(\boldsymbol{r}, |V_\mathrm{s}|)}{\mathrm{Re}\tilde{S}_{\boldsymbol{Q}_y}(\boldsymbol{r}, |V_\mathrm{s}|)}\right]. \tag{3.8}$$

The left column of Fig. 3.5 shows maps of the local amplitude of CB modulation $A^S_{\boldsymbol{Q}_y}(\boldsymbol{r}, |V_\mathrm{s}|)$ for $|V_\mathrm{s}| = 30$, 20 and 10 mV from the top. One can clearly see in these figures that the local amplitude of CB modulation exhibits spatial inhomogeneity on the nanometer scale, and that its spatial distribution is almost independent of bias voltage. The local phase $\varphi^S_{\boldsymbol{Q}_y}(\boldsymbol{r}, |V_\mathrm{s}|)$ shown in the middle column of Fig 3.5 also exhibit little bias voltage dependence. These local amplitude and phase having little dependency on bias voltage seem to be consistent with the nondispersive nature of the CB modulation.

To investigate the nature of disorders contained in the modulation, it is convenient to demodulate the analytic signal $\tilde{S}_{\boldsymbol{Q}_y}(\boldsymbol{r}, |V_\mathrm{s}|)$ by regarding a reference wave vector $\boldsymbol{Q}_y$,

$$\tilde{\boldsymbol{\mathcal{S}}}_{\boldsymbol{Q}_y}(\boldsymbol{r}, |V_\mathrm{s}|) = e^{-i\boldsymbol{Q}_y\cdot\boldsymbol{r}}\tilde{S}_{\boldsymbol{Q}_y}(\boldsymbol{r}, |V_\mathrm{s}|). \tag{3.9}$$

The local phase of this demodulated analytic signal gives the demodulated phase,

$$\psi^S_{\boldsymbol{Q}_y}(\boldsymbol{r}, |V_\mathrm{s}|) = \arctan\left[\frac{\mathrm{Im}\tilde{\boldsymbol{\mathcal{S}}}_{\boldsymbol{Q}_y}(\boldsymbol{r}, |V_\mathrm{s}|)}{\mathrm{Re}\tilde{\boldsymbol{\mathcal{S}}}_{\boldsymbol{Q}_y}(\boldsymbol{r}, |V_\mathrm{s}|)}\right], \tag{3.10}$$

which is related to the local phase $\varphi^S_{\boldsymbol{Q}_y}(\boldsymbol{r}, |V_\mathrm{s}|)$ in the following equation:

$$\begin{aligned}\tilde{S}(\boldsymbol{r}, |V_\mathrm{s}|) &= A^S_{\boldsymbol{Q}_y}(\boldsymbol{r}, |V_\mathrm{s}|)\exp\left[i\varphi^S_{\boldsymbol{Q}_y}(\boldsymbol{r}, |V_\mathrm{s}|)\right] \\ &= A^S_{\boldsymbol{Q}_y}(\boldsymbol{r}, |V_\mathrm{s}|)\exp\left\{i\left[\boldsymbol{Q}_y\cdot\boldsymbol{r} + \psi^S_{\boldsymbol{Q}_y}(\boldsymbol{r}, |V_\mathrm{s}|)\right]\right\}. \end{aligned} \tag{3.11}$$

In the maps of local phase $\varphi^S_{\boldsymbol{Q}_y}(\boldsymbol{r}, |V_\mathrm{s}|)$, one can see some edge dislocations; an extra single period is inserted into the non-distorted ideal lattice of CB

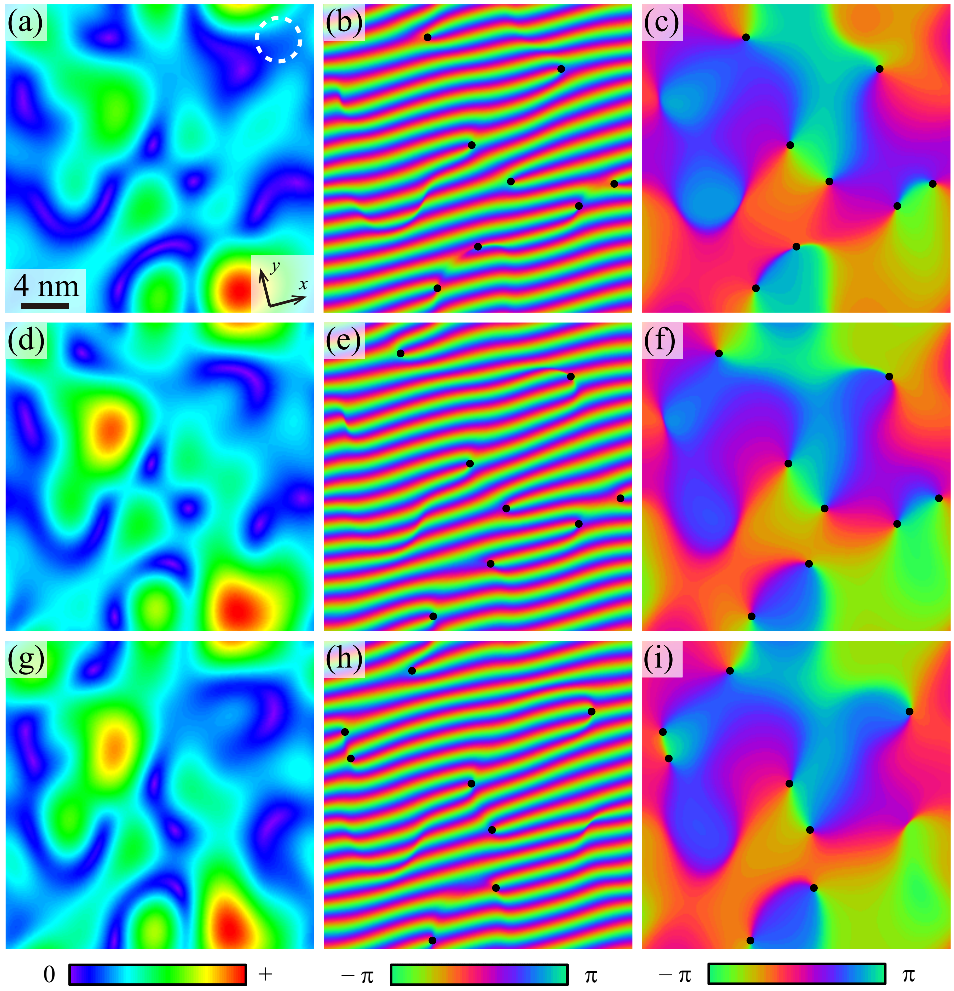


FIGURE 3.5: Local amplitude $A^{S}_{\boldsymbol{Q}_y}(\boldsymbol{r}, |V_{\mathrm{s}}|)$ (left column), local phase $\varphi^{S}_{\boldsymbol{Q}_y}(\boldsymbol{r}, |V_{\mathrm{s}}|)$ (middle column), and demodulated phase $\psi^{S}_{\boldsymbol{Q}_y}(\boldsymbol{r}, |V_{\mathrm{s}}|)$ (right column) of CB modulation: (a)–(c) for $|V_{\mathrm{s}}| = 30$ mV, (d)–(f) for $|V_{\mathrm{s}}| = 20$ mV, and (g)–(i) for $|V_{\mathrm{s}}| = 10$ mV. The dashed circle in (a) indicates the course graining length scale, and black dots in phase maps indicate edge dislocation cores.

modulation like a wedge towards the dislocation cores (black dots). At these dislocation cores, the local amplitude of CB modulation $A^{S}_{\boldsymbol{Q}_y}(\boldsymbol{r}, |V_{\mathrm{s}}|)$ tends to zero, and the demodulated phase field $\psi^{S}_{\boldsymbol{Q}_y}(\boldsymbol{r}, |V_{\mathrm{s}}|)$ shown in the right column of Fig. 3.5 exhibits a $+2\pi$ or $-2\pi$ phase winding around itself. These properties for dislocations in the CB modulation are similar to those reported for the pseudogap energy scale superstructure to be consistent with topological defects in smectic modulations [40]. One can see that the number and position of these topological defects are almost independent of the bias

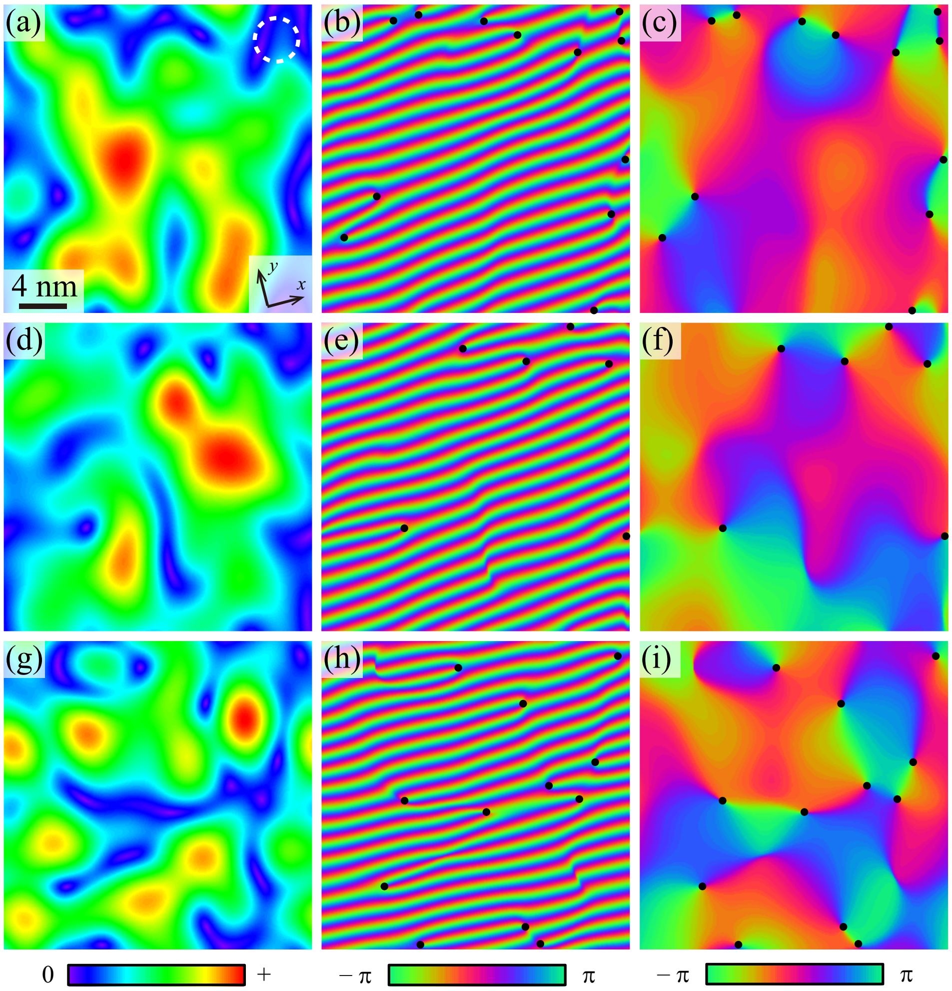


FIGURE 3.6: Local amplitude $A^{Z}_{\boldsymbol{q}_{1y}}(\boldsymbol{r}, V_{\mathrm{s}})$ (left column), local phase $\varphi^{Z}_{\boldsymbol{q}_{1y}}(\boldsymbol{r}, V_{\mathrm{s}})$ (middle column), and demodulated phase $\psi^{Z}_{\boldsymbol{q}_{1y}}(\boldsymbol{r}, V_{\mathrm{s}})$ (right column) of $\boldsymbol{q}_1$-QPI modulation: (a)–(c) for $V_{\mathrm{s}} = +30$ mV, (d)–(f) for $V_{\mathrm{s}} = +20$ mV, and (g)–(i) for $V_{\mathrm{s}} = +10$ mV. Black dots in phase maps indicate edge dislocation cores.

voltage, which coincides with the local amplitude and phase having little dependence on bias voltage. This is indicative of the energy-independent nature of CB modulation in terms of its domain structures.

### 3.2.2 Local Amplitude and Phase of $\boldsymbol{q}_1$-QPI Modulation

Next, to calculate the local amplitude and phase of the $\boldsymbol{q}_1$-QPI modulation along the $y$ direction, spatial modulations at wave vectors proximal to $\boldsymbol{q}_{1y}$ are selectively extracted from the $Z(\boldsymbol{r}, V_{\mathrm{s}})$ map in a way similar to the case of CB modulation. The $\boldsymbol{q}$-space filter used is a radial Gaussian-type mask function $e^{-(\boldsymbol{q}-\boldsymbol{q}_{1y})^2/2\Lambda^2}$ for $|\boldsymbol{q}-\boldsymbol{q}_{1y}| \leq \sqrt{2\ln 2}\Lambda$ (half width at half maximum) $\sim 0.05$ and otherwise 0. Using the complex-valued analytic signal $\tilde{Z}_{\boldsymbol{q}_{1y}}(\boldsymbol{r}, V_\mathrm{s})$ constructed (see Appendix F for the calculated analytic signals), the local amplitude and phase are given as follows:

$$A^Z_{\boldsymbol{q}_{1y}}(\boldsymbol{r}, V_\mathrm{s}) = \sqrt{\left[\mathrm{Re}\tilde{Z}_{\boldsymbol{q}_{1y}}(\boldsymbol{r}, V_\mathrm{s})\right]^2 + \left[\mathrm{Im}\tilde{Z}_{\boldsymbol{q}_{1y}}(\boldsymbol{r}, V_\mathrm{s})\right]^2}, \tag{3.12}$$

$$\varphi^Z_{\boldsymbol{q}_{1y}}(\boldsymbol{r}, V_\mathrm{s}) = \arctan\left[\frac{\mathrm{Im}\tilde{Z}_{\boldsymbol{q}_{1y}}(\boldsymbol{r}, V_\mathrm{s})}{\mathrm{Re}\tilde{Z}_{\boldsymbol{q}_{1y}}(\boldsymbol{r}, V_\mathrm{s})}\right]. \tag{3.13}$$

The demodulated phase is given by

$$\psi^{\mathcal{Z}}_{\boldsymbol{q}_{1y}}(\boldsymbol{r}, V_\mathrm{s}) = \arctan\left[\frac{\mathrm{Im}\tilde{\mathcal{Z}}_{\boldsymbol{q}_{1y}}(\boldsymbol{r}, V_\mathrm{s})}{\mathrm{Re}\tilde{\mathcal{Z}}_{\boldsymbol{q}_{1y}}(\boldsymbol{r}, V_\mathrm{s})}\right], \tag{3.14}$$

where

$$\tilde{\mathcal{Z}}_{\boldsymbol{q}_{1y}}(\boldsymbol{r}, V_\mathrm{s}) = e^{-i\boldsymbol{q}_{1y}\cdot\boldsymbol{r}}\tilde{Z}_{\boldsymbol{q}_{1y}}(\boldsymbol{r}, V_\mathrm{s}) \tag{3.15}$$

is the demodulated analytic signal. The demodulated phase $\psi^{\mathcal{Z}}_{\boldsymbol{q}_{1y}}(\boldsymbol{r}, V_\mathrm{s})$ is related to the local phase $\varphi^Z_{\boldsymbol{q}_{1y}}(\boldsymbol{r}, V_\mathrm{s})$ in the following equation:

$$\begin{aligned}\tilde{Z}_{\boldsymbol{q}_{1y}}(\boldsymbol{r}, V_\mathrm{s}) &= A^Z_{\boldsymbol{q}_{1y}}(\boldsymbol{r}, V_\mathrm{s}) \exp\left[i\varphi^Z_{\boldsymbol{q}_{1y}}(\boldsymbol{r}, V_\mathrm{s})\right] \\ &= A^Z_{\boldsymbol{q}_{1y}}(\boldsymbol{r}, V_\mathrm{s}) \exp\left\{i\left[\boldsymbol{q}_{1y}\cdot\boldsymbol{r} + \psi^{\mathcal{Z}}_{\boldsymbol{q}_{1y}}(\boldsymbol{r}, V_\mathrm{s})\right]\right\}.\end{aligned} \tag{3.16}$$

Figure 3.6 shows the maps of local amplitude $A^Z_{\boldsymbol{q}_{1y}}(\boldsymbol{r}, V_\mathrm{s})$ (left column), local phase $\varphi^Z_{\boldsymbol{q}_{1y}}(\boldsymbol{r}, V_\mathrm{s})$ (middle column) and demodulated phase $\psi^{\mathcal{Z}}_{\boldsymbol{q}_{1y}}(\boldsymbol{r}, V_\mathrm{s})$ (right column) for $V_\mathrm{s} = +30$, $+20$ and $+10$ mV from the top. The local amplitude of $\boldsymbol{q}_1$-QPI modulation is strongly inhomogeneous on the nanometer scale as in the case of CB modulation. However, a crucial difference from the CB modulation manifests itself in the energy dependence. For the $\boldsymbol{q}_1$-QPI modulation, the spatial distribution of local amplitude $A^Z_{\boldsymbol{q}_{1y}}(\boldsymbol{r}, V_\mathrm{s})$ dramatically changes with the decrease of energy. The local phase $\varphi^Z_{\boldsymbol{q}_{1y}}(\boldsymbol{r}, V_\mathrm{s})$ also shows clear energy dependence; the wavelength, or the interval between neighboring equivalent phase lines, gradually becomes shorter with lowering bias voltage, reflecting the weakly dispersive feature of $\boldsymbol{q}_1$-QPI. Finally, accompanied with

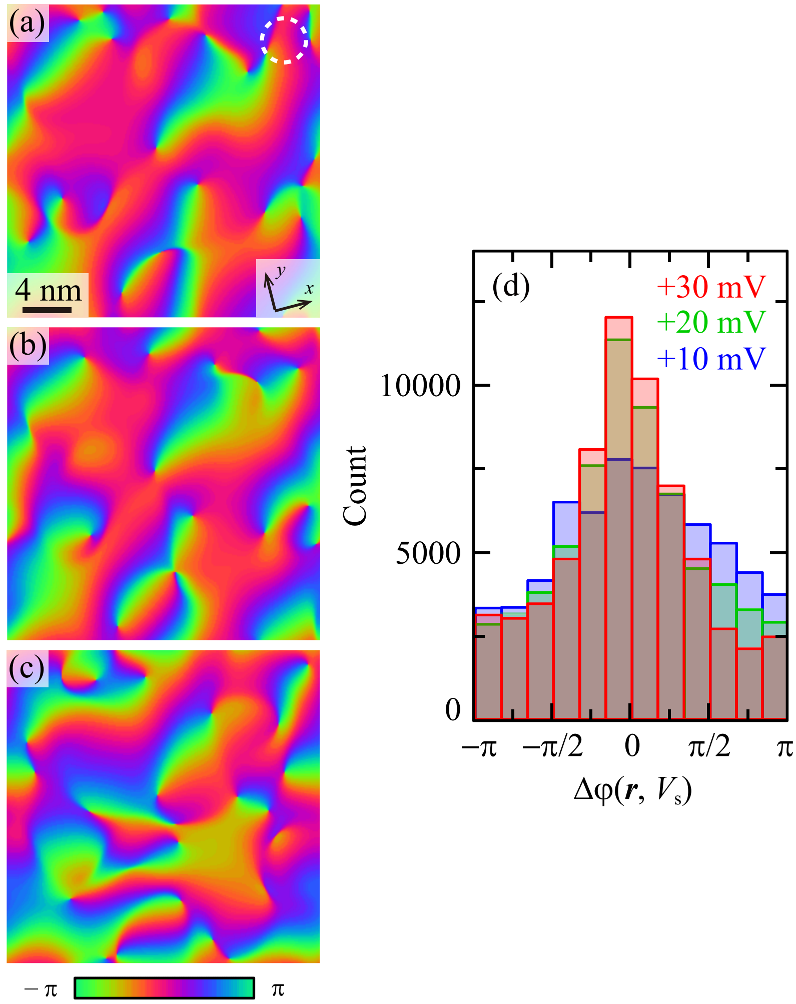


FIGURE 3.7: Local phase difference between CB and $\boldsymbol{q}_1$-QPI modulations $\Delta\varphi(\boldsymbol{r}, V_\mathrm{s})$; (a)–(c) are for $V_\mathrm{s}$ = +30, +20 and +10 mV, respectively. (d) Histograms of the local phase difference between CB and $\boldsymbol{q}_1$-QPI modulations $\Delta\varphi(\boldsymbol{r}, V_\mathrm{s})$ for $V_\mathrm{s}$ = +30, +20 and +10 mV.

the energy-depending local amplitude $A^Z_{\boldsymbol{q}_{1y}}(\boldsymbol{r}, V_\mathrm{s})$ and phase $\varphi^Z_{\boldsymbol{q}_{1y}}(\boldsymbol{r}, V_\mathrm{s})$, the number and position of the topological defects marked by black dots also change with the decrease of energy. These findings are indicative of the distinction of $\boldsymbol{q}_1$-QPI modulation from CB modulation.

## 3.3 Relationship between CB and $\boldsymbol{q}_1$-QPI Modulations

### 3.3.1 Spatial Relationship

In order to evaluate the spatial phase relationship between CB and $\boldsymbol{q}_1$-QPI modulations, I introduce a map of their local phase difference,

$$\Delta\varphi(\boldsymbol{r}, V_\mathrm{s}) \equiv \varphi^S_{\boldsymbol{Q}_y}(\boldsymbol{r}, |V_\mathrm{s}|) - \varphi^Z_{\boldsymbol{q}_{1y}}(\boldsymbol{r}, V_\mathrm{s}), \tag{3.17}$$

where $-\pi \leq \Delta\varphi(\boldsymbol{r}, V_\mathrm{s}) \leq \pi$. Figures 3.7(a)–3.7(c) show the local phase difference $\Delta\varphi(\boldsymbol{r}, V_\mathrm{s})$ for $V_\mathrm{s} = +30$, $+20$ and $+10$ mV, respectively, with their histograms shown in Fig. 3.7(d). For $V_\mathrm{s} = +30$ mV, where the wave number of $\boldsymbol{q}_1$-QPI is closest to that of CB [see Figs. 3.3(c) and 3.4(c)], one can see some nanometer-sized domains within which the local phase difference $\Delta\varphi(\boldsymbol{r}, V_\mathrm{s})$ takes on values around 0, resulting in a $\Delta\varphi(\boldsymbol{r}, V_\mathrm{s})$ distribution centered around 0, as seen in the histogram. This is indicative of the local phase matching between CB and $\boldsymbol{q}_1$-QPI modulations, notwithstanding a finite difference in their global wave numbers. The lowering of bias voltage, which brings about the larger difference between CB and $\boldsymbol{q}_1$-QPI wave numbers, leads to a shrinkage of the phase-matched domains, accompanied with the suppression of $\boldsymbol{q}_1$-QPI intensity [see Fig. 3.3(c)].

Furthermore, from a comparison between $\Delta\varphi(\boldsymbol{r}, V_\mathrm{s})$ and $A^S_{\boldsymbol{Q}_y}(\boldsymbol{r}, |V_\mathrm{s}|)$, one can see that the phase-matched domains at $V_\mathrm{s} = +30$ and $+20$ mV tend to lie where the CB modulation develops well. This finding is also supported by the radially averaged cross-correlation coefficient of $A^S_{\boldsymbol{Q}_y}(\boldsymbol{r}, |V_\mathrm{s}|) - \langle A^S_{\boldsymbol{Q}_y}(\boldsymbol{r}, |V_\mathrm{s}|)\rangle$ and $|\Delta\varphi(\boldsymbol{r}, V_\mathrm{s})| - \pi/2$ shown in Fig. 3.8(a). Here, angle brackets denote the spatial average. A negative correlation between the two quantities is clearly confirmed for $V_\mathrm{s} = +30$ and $+20$ mV, although such a correlation is unclear for $V_\mathrm{s} = +10$ mV. This is indicative of a coincidence of large $A^S_{\boldsymbol{Q}_y}(\boldsymbol{r}, |V_\mathrm{s}|)$ and $\Delta\varphi(\boldsymbol{r}, V_\mathrm{s})$ that takes on values around 0, suggesting that the local phase matching tends to occur where the CB modulation develops markedly, at least at energies where the wave number of $\boldsymbol{q}_1$-QPI is closer to that of CB.

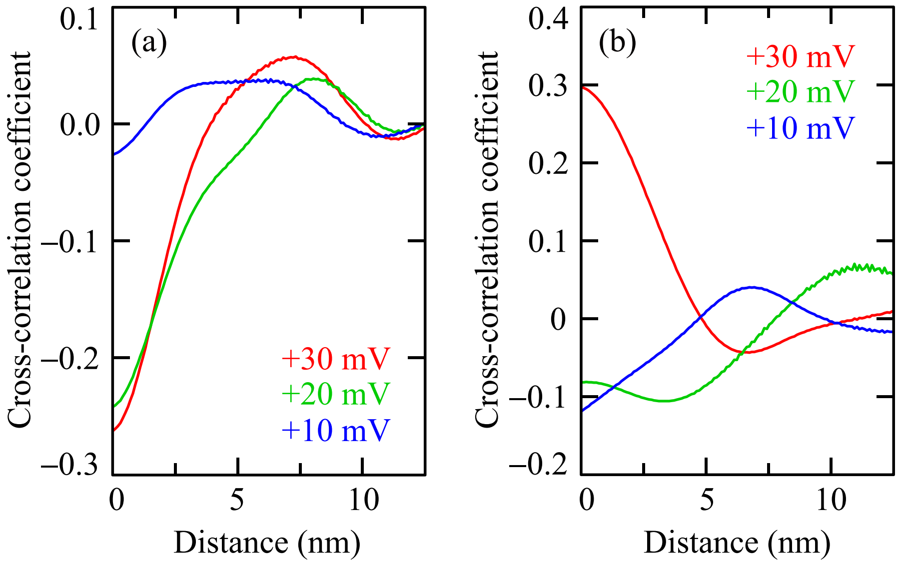


FIGURE 3.8: Radial average of normalized cross-correlation coefficients: (a) for $A^S_{\boldsymbol{Q}_y}(\boldsymbol{r}, |V_\mathrm{s}|) - \langle A^S_{\boldsymbol{Q}_y}(\boldsymbol{r}, |V_\mathrm{s}|)\rangle$ and $|\Delta\varphi(\boldsymbol{r}, V_\mathrm{s})| - \pi/2$ and (b) for $A^S_{\boldsymbol{Q}_y}(\boldsymbol{r}, |V_\mathrm{s}|) - \langle A^S_{\boldsymbol{Q}_y}(\boldsymbol{r}, |V_\mathrm{s}|)\rangle$ and $A^Z_{\boldsymbol{q}_{1y}}(\boldsymbol{r}, V_\mathrm{s}) - \langle A^Z_{\boldsymbol{q}_{1y}}(\boldsymbol{r}, V_\mathrm{s})\rangle$.

Moreover, by comparing $A^S_{\boldsymbol{Q}_y}(\boldsymbol{r}, |V_\mathrm{s}|)$ and $A^Z_{\boldsymbol{q}_{1y}}(\boldsymbol{r}, V_\mathrm{s})$ for $V_\mathrm{s} = +30$ mV, one can see that the regions where CB modulation develops well also exhibit large local amplitude of $\boldsymbol{q}_1$-QPI. The radially averaged cross-correlation coefficient of $A^S_{\boldsymbol{Q}_y}(\boldsymbol{r}, |V_\mathrm{s}|) - \langle A^S_{\boldsymbol{Q}_y}(\boldsymbol{r}, |V_\mathrm{s}|)\rangle$ and $A^Z_{\boldsymbol{q}_{1y}}(\boldsymbol{r}, V_\mathrm{s}) - \langle A^Z_{\boldsymbol{q}_{1y}}(\boldsymbol{r}, V_\mathrm{s})\rangle$ shown in Fig. 3.8(b) also supports this observation; a positive correlation between the two quantities is confirmed at least for $V_\mathrm{s} = +30$ mV, where the wave number of $\boldsymbol{q}_1$-QPI is closest to that of CB.

The spatial relationship between CB and $\boldsymbol{q}_1$-QPI modulations described above is suggestive of their interplay. Notably, the significant interplay is confirmed at $\boldsymbol{q}_1$-QPI wave vector of $\boldsymbol{q}_{1y} \sim \boldsymbol{Q}_y$.

### 3.3.2 Superposition of CB and $\boldsymbol{q}_1$-QPI Modulations

The local phase matching between CB and $\boldsymbol{q}_1$-QPI modulations observed for positive bias voltages also provides a convincing explanation on the origin of asymmetric Fourier intensity at $q_y \sim 1/4$ in $|\tilde{G}(\boldsymbol{q}, V_\mathrm{s})|$ [Fig. 3.2(e)]. Based on the antisymmetric nature of the QPI modulation described in Section 3.1, we can infer that the CB and $\boldsymbol{q}_1$-QPI modulations tend to be antiphase with

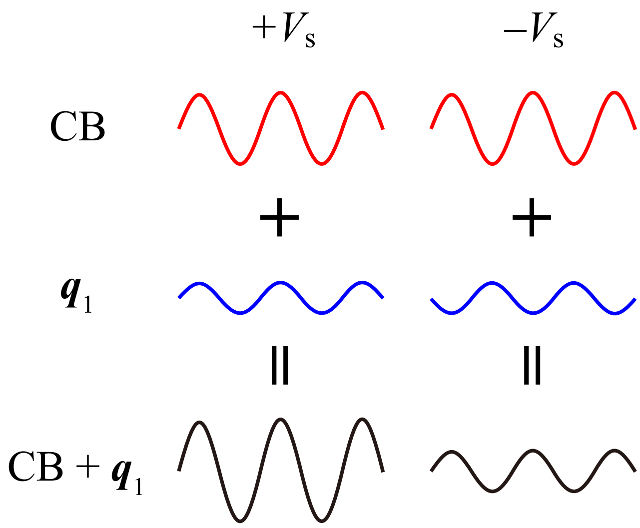


FIGURE 3.9: Schematics of superposition of CB and $\boldsymbol{q}_1$-QPI modulations, resulting in constructive and destructive interference in the LDOS for positive and negative bias voltages, respectively.

each other for negative bias voltages, while in-phase for positive bias voltages. This leads to constructive and destructive interferences of CB and $\boldsymbol{q}_1$-QPI modulations in $G(\boldsymbol{r}, V_\mathrm{s})$ for positive and negative bias voltages, respectively, bringing about an asymmetric intensity at $q_y \sim 1/4$ in $|\tilde{G}(\boldsymbol{q}, V_\mathrm{s})|$ with respect to the inversion of bias polarity, as shown in Fig. 3.9.

### 3.3.3 Interplay between CB and $\boldsymbol{q}_1$-QPI Modulations

A possible scenario for the interplay between CB and $\boldsymbol{q}_1$-QPI modulations is that the region wherein CB modulation develops well serves as an effective scattering medium for the Bogoliubov quasiparticles on the Fermi arc, inducing the $\boldsymbol{q}_1$-QPI modulation pinned by the lattice of CB modulation.

It was also confirmed in the present work that the significant interplay seems to occur at $\boldsymbol{q}_1$-QPI wave vector of $\boldsymbol{q}_{1y} \sim \boldsymbol{Q}_y$. The quasiparticle states supporting $\boldsymbol{q}_1$-QPI modulation with this wave vector live in the vicinity of the Fermi arc tips, around which the Fermi surface intersects the antiferromagnetic zone boundary. Therefore, the present finding suggests that these intersections, or the so-called "hot spots," seem to be responsible for the CB modulation, to be consistent with the scenario of CDW and/or PDW originating from the hot spots [54, 67, 68].

As presented in Section 1.3.2, the probability of quasiparticle scatterings off a given scatterer is characterized by the coherence factor, which is sensitive to whether the sign of the order parameter $\Delta_{\boldsymbol{k}}$ is preserved or reversed between initial and final states of the scattering [64]. As shown in Table 1.1 in page 8, sign-preserving scatterings at $\boldsymbol{q}_1$, $\boldsymbol{q}_4$ and $\boldsymbol{q}_5$ are induced by resonant or Andreev scatterers, while sign-reversing scatterings at $\boldsymbol{q}_2$, $\boldsymbol{q}_3$, $\boldsymbol{q}_6$ and $\boldsymbol{q}_7$ are induced by weak scalar scatterers. According to the coherence factor effects, it can be inferred that a PDW or a CDW accompanied with PDW will be a possible origin of the CB modulation as they could involve a pair potential spatially modulated in the amplitude that will serve as Andreev scatterers for Bogoliubov quasiparticles to enhance the $\boldsymbol{q}_1$ component. This scenario seems to be consistent with the recent STM/STS and SJTM experiments suggesting that the $d$-wave superconductivity coexists with a PDW and/or a CDW accompanied with PDW [77,81,82], which is also anticipated by some theoretical works [67–69].

# Chapter 4

# Summary

In the present STM/STS study, constant-height $dI/dV$ imaging was performed at 7 K on the underdoped $Bi_2Sr_2CaCu_2O_{8+x}$ with a hole doping level of $p \sim 0.12$ ($T_c = 76$ K). Spatial maps of $dI/dV$, or $G(\boldsymbol{r}, V_s)$ maps were measured at low bias voltages in a range of $|V_s| \leq 30$ mV to examine the spatial relationship between CB and QPI modulations, which are characteristic for the low-energy electronic states.

The CB and QPI modulations were most satisfactorily separated from each other by constructing $S(\boldsymbol{r}, |V_s|)$ and $Z(\boldsymbol{r}, V_s)$ maps, which give the symmetric and antisymmetric components in $G(\boldsymbol{r}, \pm V_s)$ maps, respectively. This is indicative of the coexistence of these two superstructures in identical regions of the $CuO_2$ plane. Simultaneously, it was confirmed that the dispersive QPI modulation is almost antisymmetric with respect to the sign change of bias voltage, while the nondispersive CB modulation is almost symmetric.

The local amplitude and phase are then evaluated for CB and $\boldsymbol{q}_1$-QPI modulations having similar wave vectors. Both of these superstructures contain disorders characterized by the topological defects, at which the edge dislocation cores live suppressing the local amplitude of the modulation. The significant difference between CB and $\boldsymbol{q}_1$-QPI modulations is found in their energy dependence; the number and positions of the topological defects for $\boldsymbol{q}_1$-QPI exhibit a clear energy dependence, while those for CB are almost independent of energy to be coincided with the almost energy-independent local amplitude and phase. These energy dependences are consistent with the dispersive and nondispersive natures of QPI and CB modulations, respectively.

Furthermore, it was also found that there exists a settled spatial phase relationship between CB and $\boldsymbol{q}_1$-QPI modulations; these two superstructures form nanometer-sized domains within which they tend to be in-phase and antiphase for positive and negative bias voltages, respectively. At the energy where the wave number of $\boldsymbol{q}_1$-QPI is closest to that of CB, the local amplitude of CB modulation positively correlates not only with the degree to which the settled phase relationship is realized, but also with the local amplitude of $\boldsymbol{q}_1$-QPI modulation. As the wave number of $\boldsymbol{q}_1$-QPI goes away from that of CB with decreasing energy, these domains become smaller accompanied with the reduction of $\boldsymbol{q}_1$-QPI intensity.

These findings are suggestive of an interplay between CB and $\boldsymbol{q}_1$-QPI modulations. A prospected scenario for this interplay is that the region where CB modulation develops well serves as an effective scattering source for the SC quasiparticles on the Fermi arc to induce the $\boldsymbol{q}_1$-QPI modulation with the settled spatial phase. The significant interplay seems to occur at an energy where the dispersive $\boldsymbol{q}_1$-QPI wave vector agrees with the nondispersive CB wave vector, suggesting that the hot spots near the Fermi arc tip may be responsible for the CB modulation. In terms of the coherence factor, moreover, the $\boldsymbol{q}_1$ component arising from the sign-preserving scatterings can be enhanced by resonant or Andreev scatterers, while it is unresponsive to weak scalar and weak magnetic scatterers. Therefore, a PDW or a CDW accompanied with PDW, which can reasonably provide Andreev scatterers for Bogoliubov quasiparticles, will be a possible origin of the CB modulation.

# Appendix A

# $dI/dV$ Spectra in the Same Cleaved Surface

In the same cleaved surface where $G(\boldsymbol{r}, V_\mathrm{s})$ maps presented in Chapter 3 were measured, multiple $dI/dV$ spectra were systematically collected in the conventional way described in Section 2.2.3. Figure A.1(a) shows an atomically resolved topography of the $\mathrm{Bi_2Sr_2CaCu_2O_{8+x}}$ in the same cleaved surface but with a field of view different from Fig. 3.1. The $dI/dV$ spectra were corrected in the boxed region. They exhibit sub gaps at $|V_\mathrm{s}| \sim \pm 25$ mV$(= \Delta_\mathrm{SG}/e)$ in addition to the pseudogap peaks at larger energy scale $\Delta_\mathrm{PG}$, as can be seen in Fig. A.1(c). The pseudogap exhibits spatial inhomogeneity, with its energy size $\Delta_\mathrm{PG}$ distributed from $\sim$40 to over 100 meV on the nanometer scale [Fig. A.1(b)], whereas the sub-gap energy $\Delta_\mathrm{SG}$ is comparatively homogeneous.

Furthermore, one can also see from Fig. A.1(c) that the $dI/dV$ spectra are almost particle-hole symmetric in a low-energy region $e|V_\mathrm{s}| \leq 30$ mV, within which $G(\boldsymbol{r}, V_\mathrm{s})$ maps presented in Chapter 3 were measured. As described in Section 2.2.5, this allows the separation of CB and QPI modulations using a pair of $G(\boldsymbol{r}, \pm V_\mathrm{s})$ maps measured in constant-height mode under a setup current with the same amplitude.

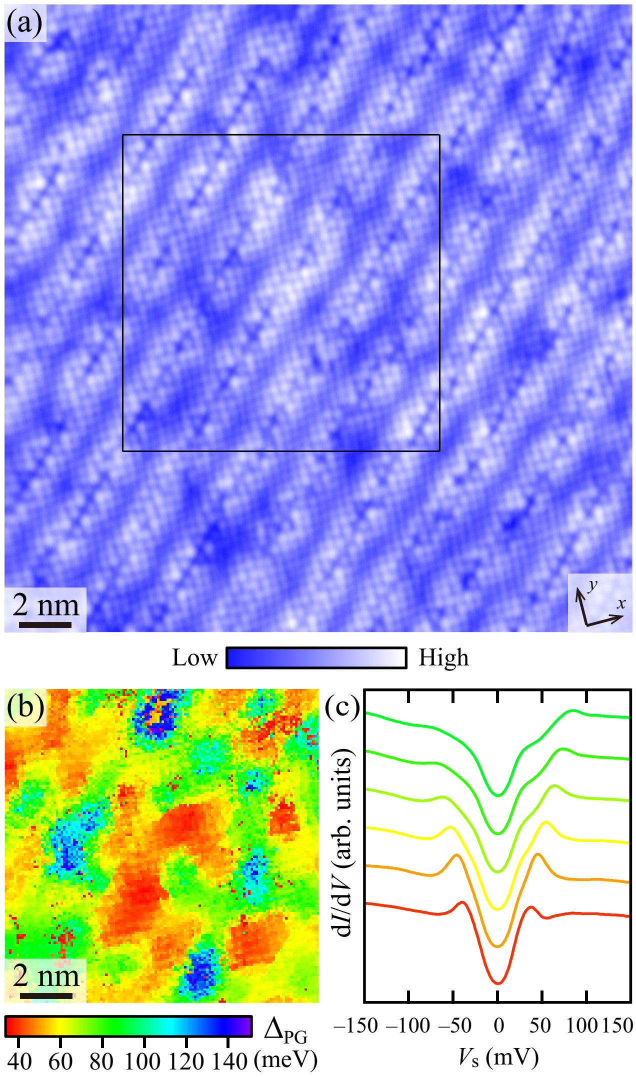


FIGURE A.1: (a) Atomically resolved topography of the underdoped $Bi_2Sr_2CaCu_2O_{8+x}$ ($p \sim 0.12$ and $T_c = 76$ K) for $V_s = +100$ mV measured at 7 K in the same cleaved surface where constant-height $dI/dV$ imaging was performed. $dI/dV$ spectra were measured on a two-dimensional dense array of measurement points within the boxed region. (b) Spatial map of the pseudogap energy $\Delta_{\mathrm{PG}}$, which was determined by the energy where each $dI/dV$ spectrum exhibits a peak of the pseudogap in the positive bias side. (c) $dI/dV$ spectra binned by $\Delta_{\mathrm{PG}}$ value. The line color of each spectrum indicates $\Delta_{\mathrm{PG}}$ value as in (b).

# Appendix B

# Energy Dependence of $G(\boldsymbol{r}, V_{\mathrm{s}})$ and $|\tilde{G}(\boldsymbol{q}, V_{\mathrm{s}})|$

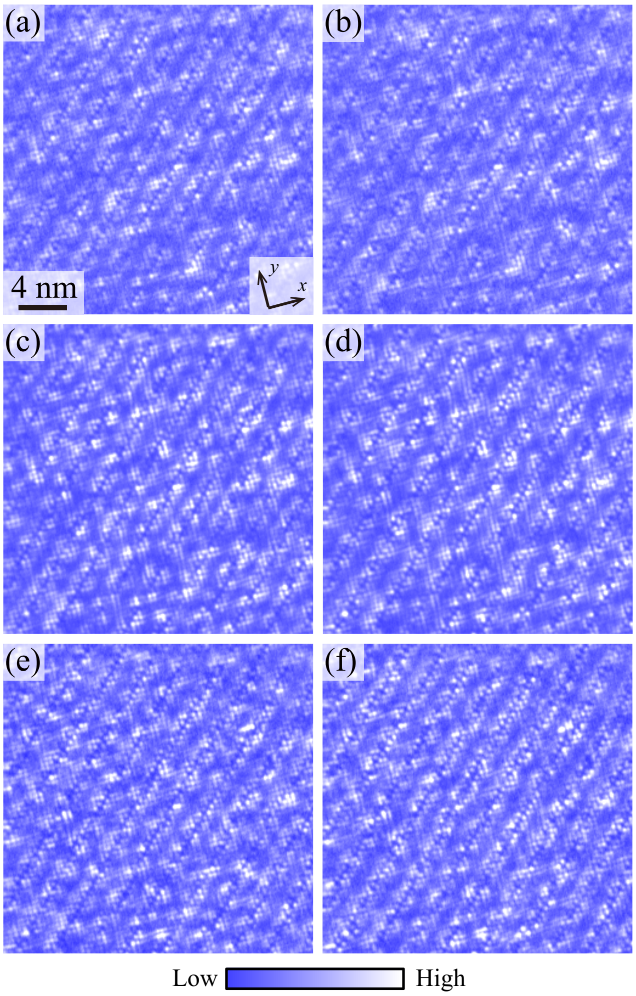


FIGURE B.1: $G(\boldsymbol{r}, V_\mathrm{s})$ maps measured at 7 K in underdoped $Bi_2Sr_2CaCu_2O_{8+x}$ ($p \sim 0.12$ and $T_\mathrm{c} = 76$ K); (a)–(f) are for $V_\mathrm{s} = +30$, $-30$, $+20$, $-20$, $+10$, and $-10$ mV. Each pair of $G(\boldsymbol{r}, \pm V_\mathrm{s})$ maps were measured under a setup current with the same amplitude.

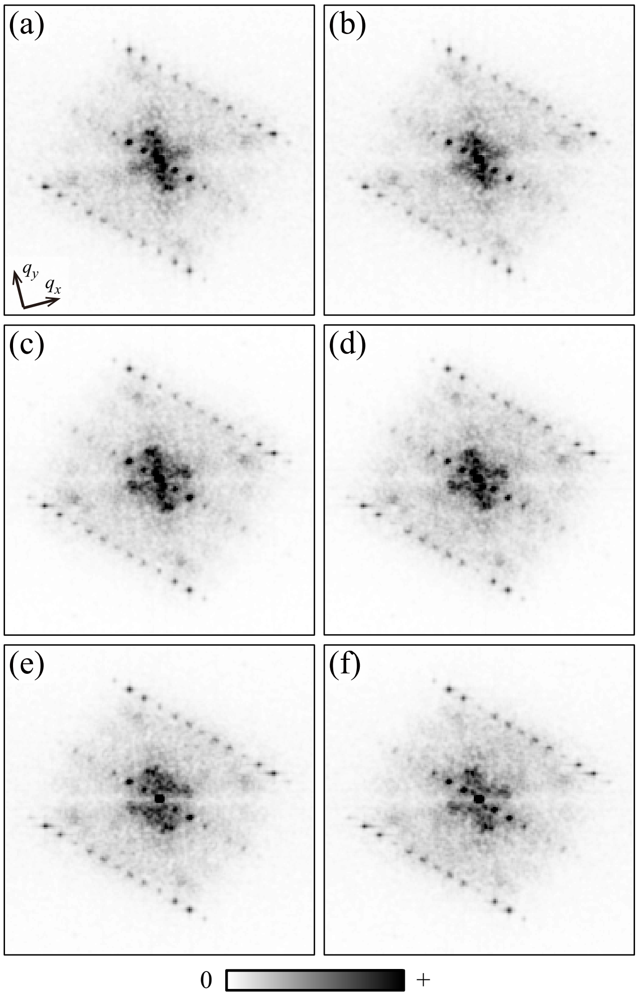


FIGURE B.2: FT maps $|\tilde{G}(\boldsymbol{q}, V_\mathrm{s})|$; (a)–(f) are for $V_\mathrm{s}$ = +30, −30, +20, −20, +10, and −10 mV. For each FT map, 3 × 3 Gaussian filter was applied two times.

# Appendix C

# Energy Dependence of $Z(\boldsymbol{r}, V_{\mathrm{s}})$ and $|\tilde{Z}(\boldsymbol{q}, V_{\mathrm{s}})|$

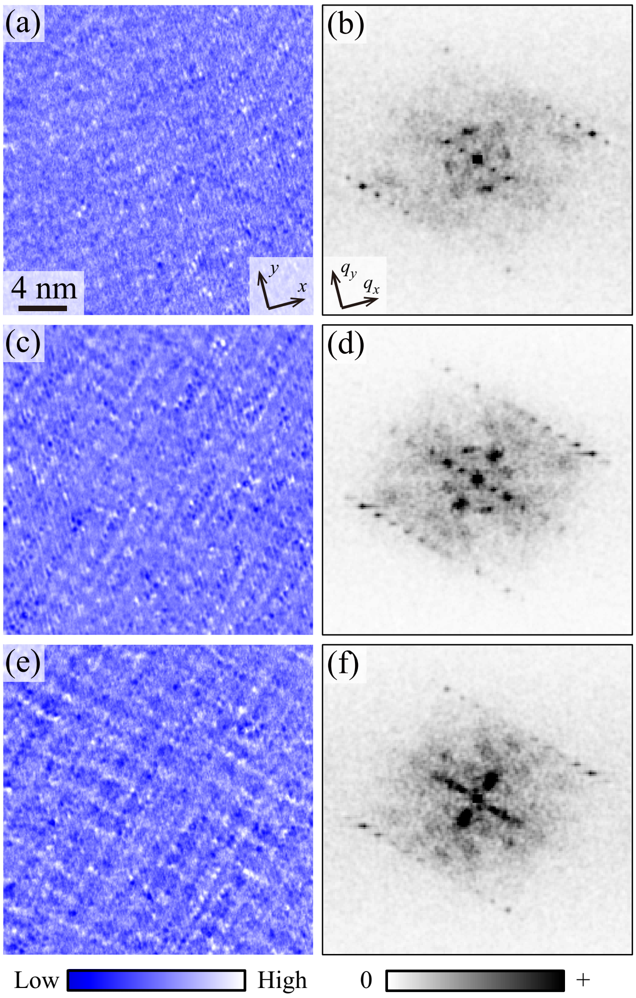


FIGURE C.1: $Z(\boldsymbol{r}, V_{\rm s})$ maps (left column) and the FT maps $|\tilde{Z}(\boldsymbol{q}, V_{\rm s})|$ (right column): (a), (b) for $V_{\rm s} = +30$ mV, (c), (d) for $V_{\rm s} = +20$ mV, and (e), (f) for $V_{\rm s} = +10$ mV. For each FT map, $3 \times 3$ Gaussian filter was applied two times.

# Appendix D

# Energy Dependence of $S(\boldsymbol{r}, |V_\mathrm{S}|)$ and $|\tilde{S}(\boldsymbol{q}, |V_\mathrm{S}|)|$

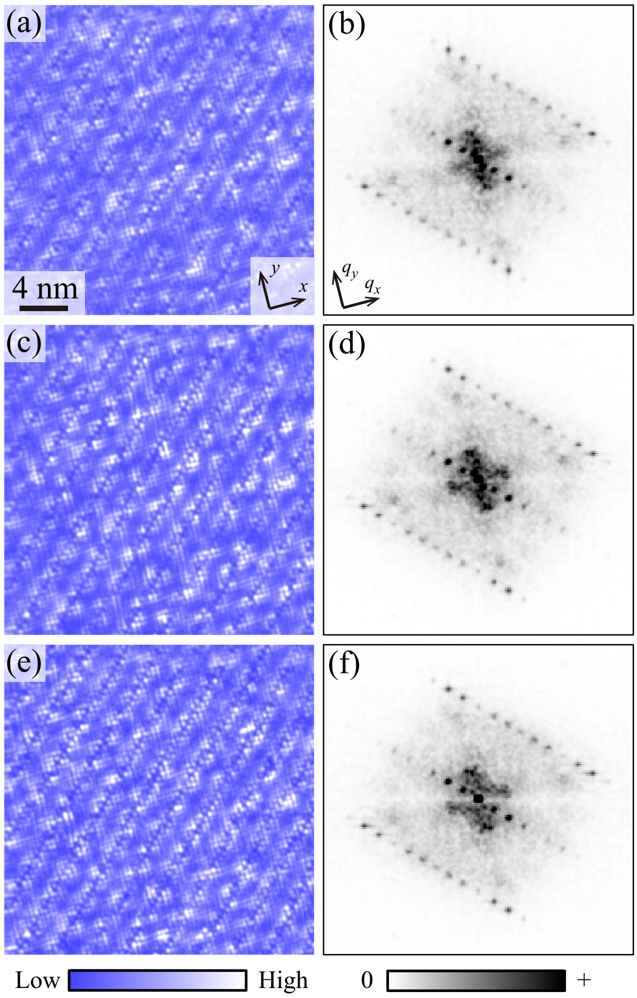


FIGURE D.1: $S(\boldsymbol{r}, |V_s|)$ maps (left column) and the FT maps $|\tilde{S}(\boldsymbol{q}, |V_s|)|$ (right column): (a), (b) for $|V_s| = 30$ mV, (c), (d) for $|V_s| = 20$ mV, and (e), (f) for $|V_s| = 10$ mV. For each FT map, $3 \times 3$ Gaussian filter was applied two times.

# Appendix E

# Determining CB and $\boldsymbol{q}_1$-QPI Wave Vectors

Conventionally, the wave vector of an electronic superstructure in a conductance map $M(\boldsymbol{r}, V_{\mathrm{s}})$ has been determined by the $\boldsymbol{q}$-space coordinate where the Fourier amplitude $|\tilde{M}(\boldsymbol{q}, V_{\mathrm{s}})|$ exhibits a peak corresponding to the superstructure. However, the Fourier amplitude-defined wave vector cannot always be a reliable measure of the modulation wave vector since the inhomogeneity of the modulation can split the observed Fourier peaks.

Mesaros *et al.* introduced the demodulation phase residue minimization technique to evaluate the wave vectors of inhomogeneous *d*FF-DW exhibiting discommensurations in their phases [35]. In this technique, the demodulated analytic signal

$$\tilde{\mathcal{M}}_{\boldsymbol{q}}(\boldsymbol{r}, V_{\mathrm{s}}) = e^{-i\boldsymbol{q}\cdot\boldsymbol{r}} \tilde{M}_{\boldsymbol{q}}(\boldsymbol{r}, V_{\mathrm{s}}) \tag{E.1}$$

at each trial wave vector $\boldsymbol{q}$ around the Fourier spot of interest is evaluated by using a measure called the demodulation phase residue $\boldsymbol{R}_{\boldsymbol{q}} = \left(R^x_{\boldsymbol{q}}, R^y_{\boldsymbol{q}}\right)$,

$$R^x_{\boldsymbol{q}} = \int \frac{d^2\boldsymbol{r}}{L^2} \mathrm{Re}\left[\tilde{\mathcal{M}}^*_{\boldsymbol{q}}(\boldsymbol{r}, V_{\mathrm{s}})(-i\partial_x)\tilde{\mathcal{M}}_{\boldsymbol{q}}(\boldsymbol{r}, V_{\mathrm{s}})\right], \tag{E.2}$$

$$R^y_{\boldsymbol{q}} = \int \frac{d^2\boldsymbol{r}}{L^2} \mathrm{Re}\left[\tilde{\mathcal{M}}^*_{\boldsymbol{q}}(\boldsymbol{r}, V_{\mathrm{s}})(-i\partial_y)\tilde{\mathcal{M}}_{\boldsymbol{q}}(\boldsymbol{r}, V_{\mathrm{s}})\right], \tag{E.3}$$

where $L$ is the size of the field of view. Then, the wave vector $\boldsymbol{q} = \boldsymbol{Q}$ for which

$$|\boldsymbol{R}_{\boldsymbol{q}}| = \sqrt{\left(R^x_{\boldsymbol{q}}\right)^2 + (R^y_{\boldsymbol{q}})^2} \tag{E.4}$$

takes a minimum value is adopted as the modulation wave vector. This phase-optimized wave vector gives a linear fit $\boldsymbol{Q}\cdot\boldsymbol{r}+\varphi$ to the phase argument of the measured superstructure, and is robust to the inhomogeneity of the modulation.

In the present study, the wave vectors of CB and $\boldsymbol{q}_1$-QPI modulations along the $y$ direction were determined by using this technique. The raw FT maps and $|R_{\boldsymbol{q}}|$ maps for $S(\boldsymbol{r},|V_{\mathrm{s}}|)$ maps are shown in Fig. E.1, while those for $Z(\boldsymbol{r},V_{\mathrm{s}})$ maps are shown in Fig. E.2.

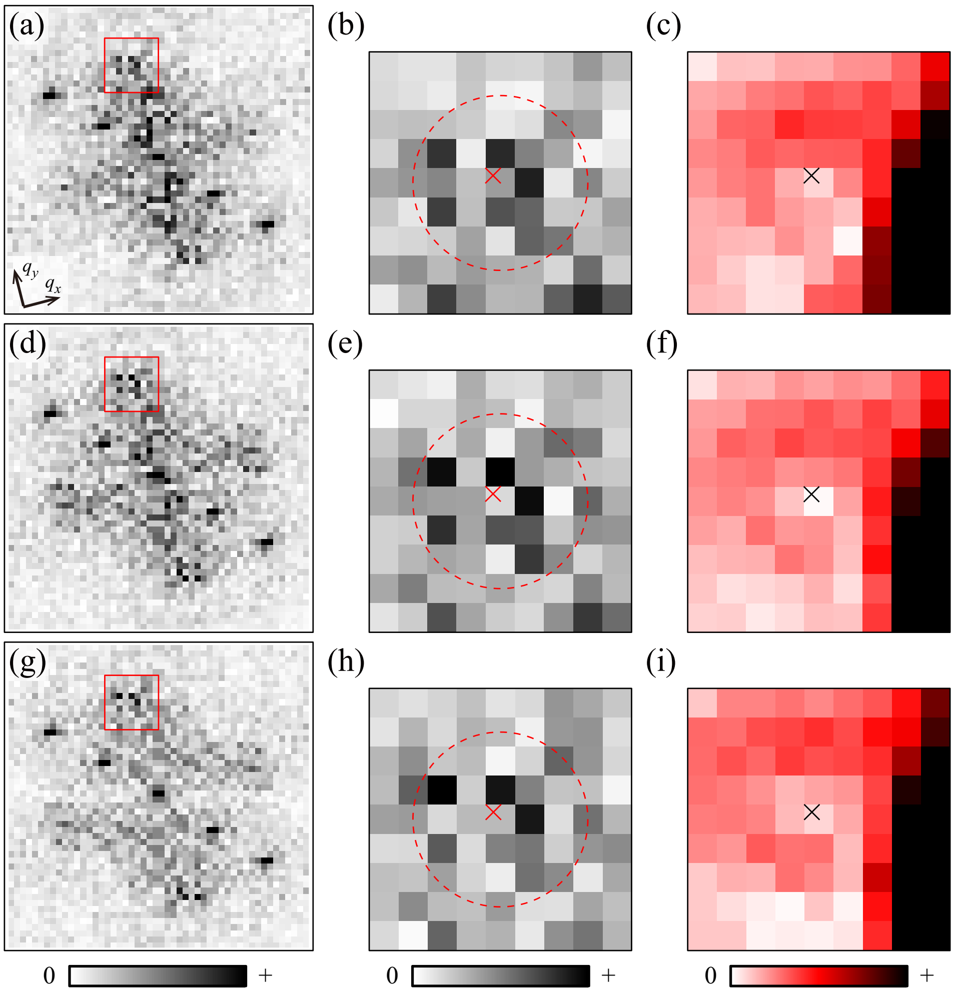


FIGURE E.1: Raw FT maps $|\tilde{S}(\boldsymbol{q}, |V_{\mathrm{s}}|)|$ in the vicinity of the origin (left column), magnified images of the boxed regions in the FT maps (middle column), and maps of the corresponding demodulation phase residue $|R_{\boldsymbol{q}}|$ (right column): (a)–(c) for $|V_{\mathrm{s}}| = 30$ mV, (d)–(f) for $|V_{\mathrm{s}}| = 20$ mV, and (g)–(i) for $|V_{\mathrm{s}}| = 10$ mV. Small crosses indicate the corresponding position of $\boldsymbol{q} = (0, 0.25) \times (2\pi/a)$. Center of each images in the middle and right columns indicates the adopted CB wave vector $\boldsymbol{Q}_y$, at which the corresponding $|R_{\boldsymbol{q}}|$ takes a minimum value. The determined wave vector is totally independent of bias voltage, and its magnitude is $|\boldsymbol{Q}_y| = 0.245$. Dashed circles in the middle column indicate the region within the full width at half maximum $2\sqrt{2\ln 2}\Lambda \sim 0.1$ of the radial Gaussian-type mask function $e^{-(\boldsymbol{q}-\boldsymbol{Q}_y)^2/2\Lambda^2}$ adopted.

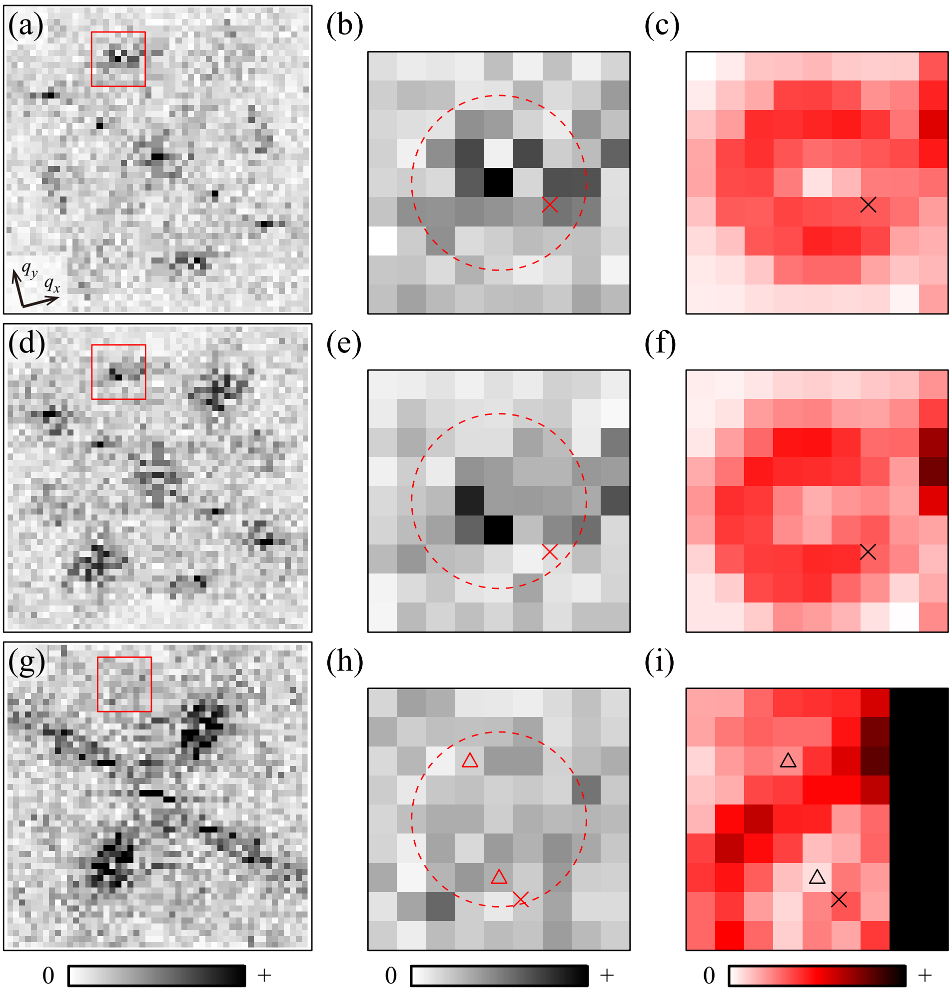


FIGURE E.2: Raw FT maps $|\tilde{Z}(\boldsymbol{q}, V_\mathrm{s})|$ in the vicinity of the origin (left column), magnified images of the boxed regions in the FT maps (middle column), and maps of the corresponding demodulation phase residue $|R_{\boldsymbol{q}}|$ (right column): (a)–(c) for $V_\mathrm{s} = +30$ mV, (d)–(f) for $V_\mathrm{s} = +20$ mV, and (g)–(i) for $V_\mathrm{s} = +10$ mV. Small crosses indicate the corresponding position of $\boldsymbol{q} = (0, 0.25) \times (2\pi/a)$. Center of each images in the middle and right columns indicates the adopted $\boldsymbol{q}_1$-QPI wave vector $\boldsymbol{q}_{1y}$, at which the corresponding $|R_{\boldsymbol{q}}|$ takes a minimum value for $V_\mathrm{s} = +30$ and $+20$ mV. For $V_\mathrm{s} = +10$ mV, however, $|R_{\boldsymbol{q}}|$ exhibits two minima marked by small triangles, and thus their mean wave vector was adopted as $\boldsymbol{q}_{1y}$. The determined wave vector depends on energy, and its magnitude is $|\boldsymbol{q}_{1y}| = 0.268$, 0.282 and 0.292 for $V_\mathrm{s} = +30$, $+20$ and $+10$ mV, respectively. Dashed circles in the middle column indicate the region within the full width at half maximum $2\sqrt{2\ln 2}\Lambda \sim 0.1$ of the radial Gaussian-type mask function $e^{-(\boldsymbol{q}-\boldsymbol{q}_{1y})^2/2\Lambda^2}$ adopted.

# Appendix F

# Analytic Signals of CB and $\boldsymbol{q}_1$-QPI Modulations

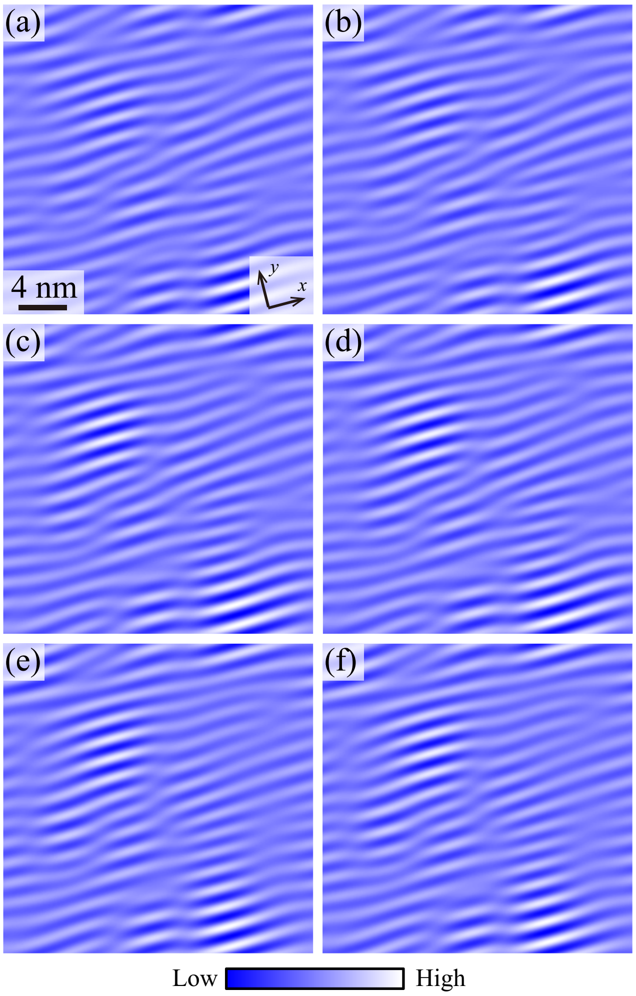


FIGURE F.1: Real and imaginary parts of the analytic signal $\mathrm{Re}\tilde{S}_{\boldsymbol{Q}_y}(\boldsymbol{r}, |V_\mathrm{s}|)$ (left column) and $\mathrm{Im}\tilde{S}_{\boldsymbol{Q}_y}(\boldsymbol{r}, |V_\mathrm{s}|)$ (right column) of CB modulation: (a), (b) for $|V_\mathrm{s}| = 30$ mV, (c), (d) for $|V_\mathrm{s}| = 20$ mV, and (e), (f) for $|V_\mathrm{s}| = 10$ mV.

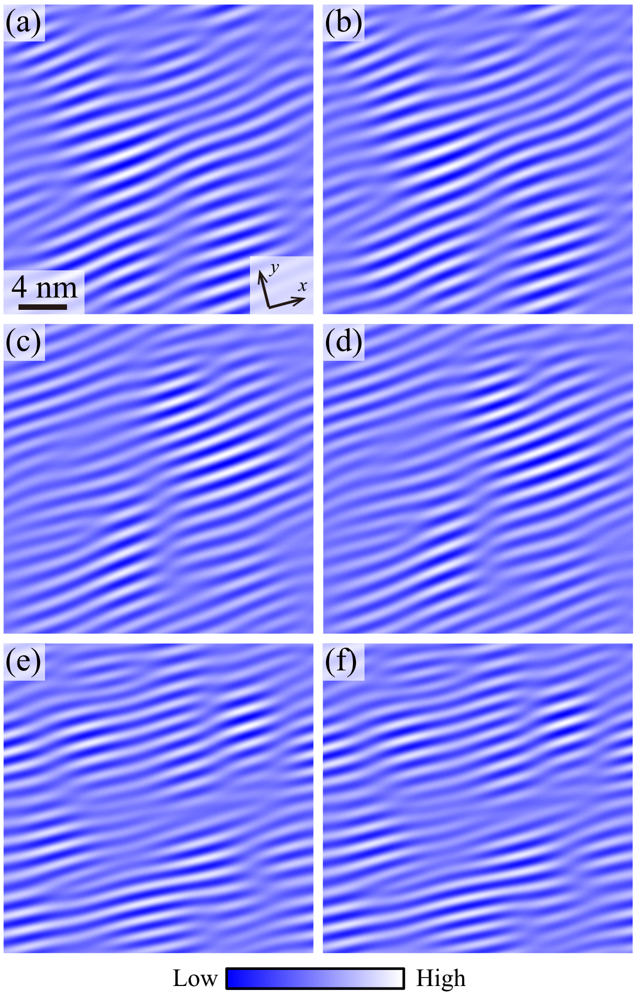


FIGURE F.2: Real and imaginary parts of the analytic signal $\mathrm{Re}\tilde{Z}_{\boldsymbol{q}_{1y}}(\boldsymbol{r}, V_\mathrm{s})$ (left column) and $\mathrm{Im}\tilde{Z}_{\boldsymbol{q}_{1y}}(\boldsymbol{r}, V_\mathrm{s})$ (right column) of $\boldsymbol{q}_1$-QPI modulation: (a), (b) for $V_\mathrm{s} = +30$ mV, (c), (d) for $V_\mathrm{s} = +20$ mV, and (e), (f) for $V_\mathrm{s} = +10$ mV.

# Appendix G

# Low-energy LDOS without Strong QPI Modulation

Low-bias $G(\boldsymbol{r}, V_\mathrm{s})$ maps presented in Chapter 3 contain QPI modulation with detectable intensities. However, there is another case where strong signal of QPI modulation is not included in low-bias $G(\boldsymbol{r}, V_\mathrm{s})$ maps, as in the data acquired in the underdoped $\mathrm{Bi_2Sr_2CaCu_2O_{8+x}}$ ($p \sim 0.11$ and $T_\mathrm{c} = 68$ K) shown below (see Fig. 2.3 for the diamagnetic transition curve).

The constant-height $dI/dV$ imaging was performed in the same field of view where atomically-resolved current image shown in Fig. G.1 was measured. The low-bias $G(\boldsymbol{r}, V_\mathrm{s})$ maps for $V_\mathrm{s} = \pm 30$, $\pm 20$, and $\pm 10$ mV are shown in Fig. G.2, with their FT maps $|\tilde{G}(\boldsymbol{q}, V_\mathrm{s})|$ shown in Fig. G.3. The real-space maps exhibit a checkerboardlike pattern, yielding the corresponding Fourier spots on the $q_x$ and $q_y$ axes in the FT maps. On the other hand, the $Z(\boldsymbol{r}, V_\mathrm{s})$ maps and their FT maps $|\tilde{Z}(\boldsymbol{q}, V_\mathrm{s})|$ shown in Fig. G.4 do not exhibit a clear signature of QPI modulation. The line cuts of FT maps $|\tilde{Z}(\boldsymbol{q}, V_\mathrm{s})|$ along the $q_x$ axis shown in Fig. G.5(b) also do not show any detectable peak corresponding to the $\boldsymbol{q}_1$-QPI. In this case, the intensity of Fourier peaks at $q_x \sim 1/4$ in the line cuts of FT maps $|\tilde{G}(\boldsymbol{q}, V_\mathrm{s})|$ is almost symmetric with respect to the inversion of bias polarity [Fig. G.5(a)], reflecting the nature of the CB modulation itself.

Although it is unclear what determines whether the strong QPI modulation is observed or not, the absence of QPI modulation in the present case seems

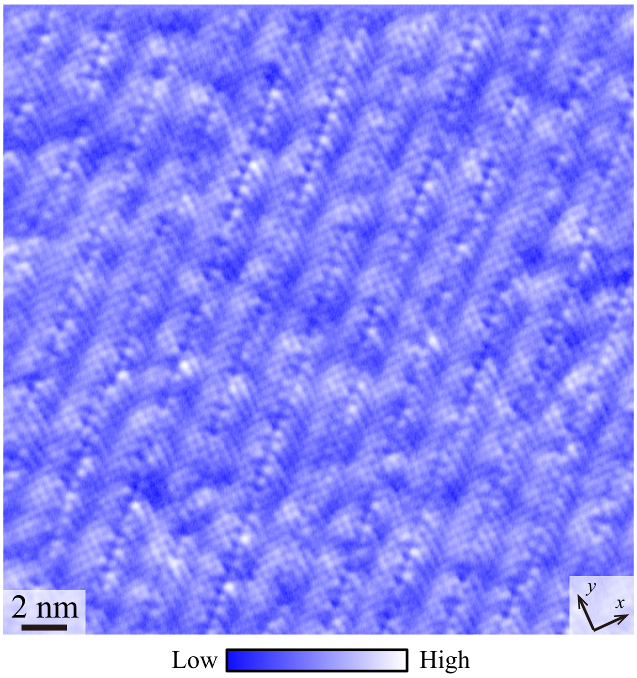


FIGURE G.1: Atomically resolved current image of the underdoped $Bi_2Sr_2CaCu_2O_{8+x}$ ($p \sim 0.11$ and $T_c = 68$ K) for $V_s = +100$ mV measured at 7 K.

to be due to some momentum-independent smearing effects such as a short life time of the Bogoliubov quasiparticles since all of the seven independent QPI components are weak, as shown in Fig. G.4.

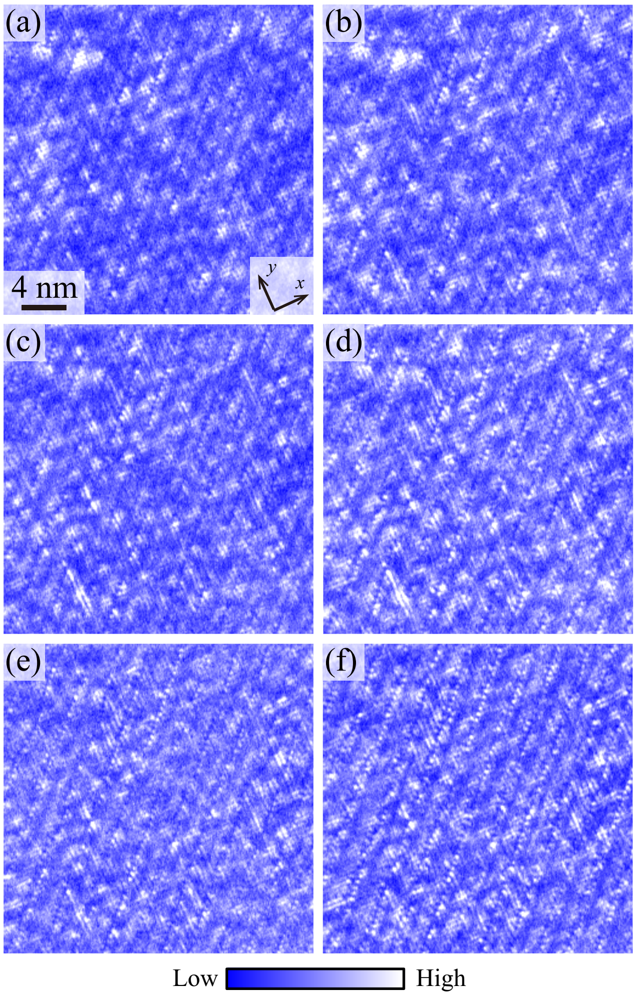


FIGURE G.2: $G(\boldsymbol{r}, V_\mathrm{s})$ maps measured at 7 K in underdoped $Bi_2Sr_2CaCu_2O_{8+x}$ ($p \sim 0.11$ and $T_\mathrm{c} = 68$ K); (a)–(f) are for $V_\mathrm{s} = +30$, $-30$, $+20$, $-20$, $+10$, and $-10$ mV. Each pair of $G(\boldsymbol{r}, \pm V_\mathrm{s})$ maps were measured under a setup current with the same amplitude.

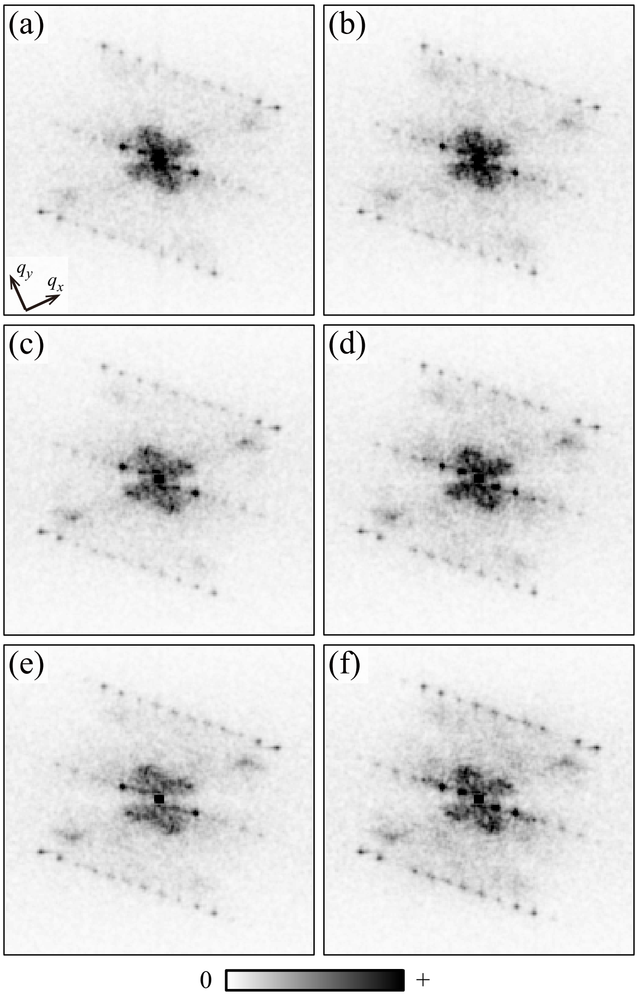


FIGURE G.3: FT maps $|\tilde{G}(\boldsymbol{q}, V_s)|$; (a)–(f) are for $V_s$ = +30, −30, +20, −20, +10, and −10 mV. For each FT map, 3 × 3 Gaussian filter was applied two times.

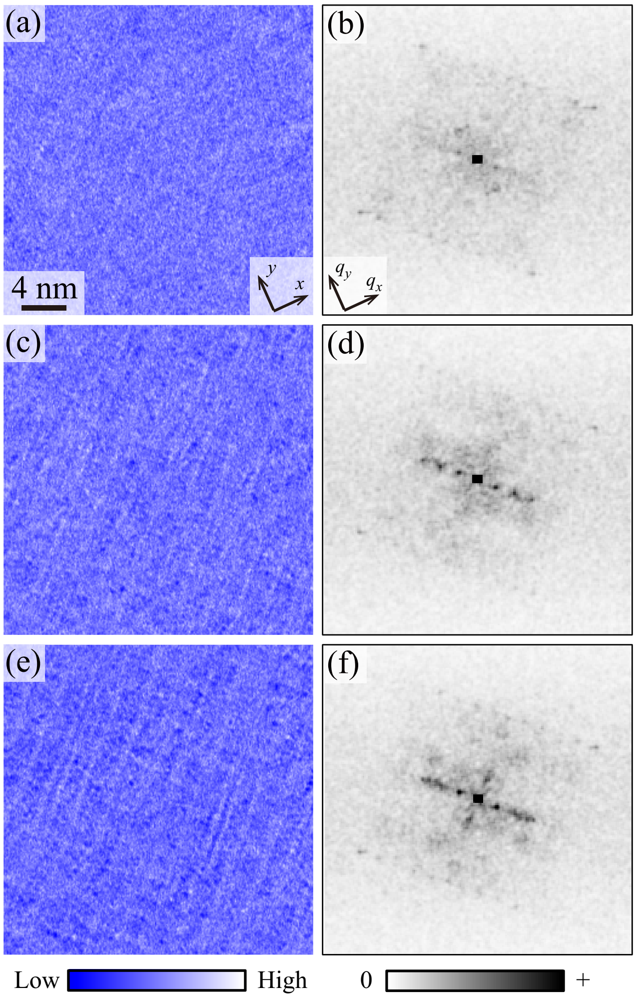


FIGURE G.4: $Z(\boldsymbol{r}, V_\mathrm{s})$ maps (left column) and the FT maps $|\tilde{Z}(\boldsymbol{q}, V_\mathrm{s})|$ (right column): (a), (b) for $V_\mathrm{s} = +30$ mV, (c), (d) for $V_\mathrm{s} = +20$ mV, and (e), (f) for $V_\mathrm{s} = +10$ mV. For each FT map, $3 \times 3$ Gaussian filter was applied two times.

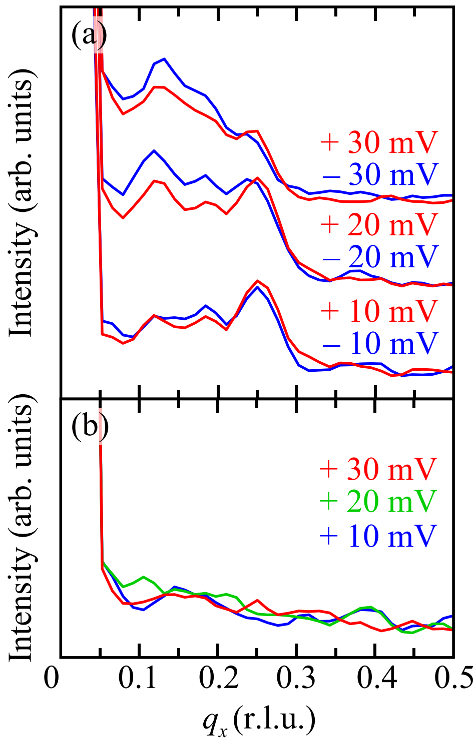


FIGURE G.5: (a) Line cuts of the FT maps $|\tilde{G}(\boldsymbol{q}, V_{\mathrm{s}})|$ on the $q_x$ axis plotted in a reciprocal lattice unit (r.l.u.) defined as $2\pi/a = 1$ for $V_{\mathrm{s}} = \pm 10$, $\pm 20$, and $\pm 30$ mV. (b) Line cuts of FT maps $|\tilde{Z}(\boldsymbol{q}, V_{\mathrm{s}})|$ on the $q_x$ axis for $V_{\mathrm{s}} = +10$, $+20$, and $+30$ mV.

# References


[1] J. G. Bednorz, and K. A. Müller, Z. Phys. B **64**, 189 (1986).

[2] B. Keimer, S. A. Kivelson, M. R. Norman, S. Uchida, and J. Zaanen, Nature **518**, 179 (2015).

[3] H. Kamerlingh Onnes, Commun. Phys. Lab. Univ. Leiden **120b**, **122b**, **124c** (1911).

[4] W. Meissner and R. Ochsenfeld, Naturwissenschaften **21**, 787 (1933).

[5] J. Bardeen, L. N. Cooper, and J. R. Schrieffer, Phys. Rev. **108**, 1175 (1957).

[6] L. N. Cooper, Phys. Rev. **104**, 1189 (1956).

[7] H. Fröhlich, Phys. Rev. **79**, 845 (1950).

[8] N. N. Bogoliubov, Il Nuovo Cimento **7**, 794 (1958).

[9] J. G. Valatin, Il Nuovo Cimento **7**, 843 (1958).

[10] M. R. Norman, H. Ding, M. Randeria, J. C. Campuzano, T. Yokoya, T. Takeuchi, T. Takahashi, T. Mochiku, K. Kadowaki, P. Guptasarma, and D. G. Hinks, Nature (London) **392**, 157 (1998).

[11] K. Tanaka, W. S. Lee, D. H. Lu, A. Fujimori, T. Fujii, Risdiana, I. Terasaki, D. J. Scalapino, T. P. Devereaux, Z. Hussain, and Z.-X. Shen, Science **314**, 1910 (2006).

[12] T. Kondo, T. Takeuchi, A. Kaminski, S. Tsuda, and S. Shin, Phys. Rev. Lett. **98**, 267004 (2007).

[13] T. Yoshida, M. Hashimoto, S. Ideta, A. Fujimori, K. Tanaka, N. Mannella, Z. Hussain, Z.-X. Shen, M. Kubota, K. Ono, S. Komiya, Y. Ando, H. Eisaki, and S. Uchida, Phys. Rev. Lett. **103**, 037004 (2009).

[14] I. Madan, T. Kurosawa, Y. Toda, M. Oda, T. Mertelj, and D. Mihailovic, Nat. Commun. **6**, 6958 (2015).

[15] R. M. Dipasupil, M. Oda, N. Momono, and M. Ido, J. Phys. Soc. Jpn.

**71**, 1535 (2002).

[16] Y. H. Liu, Y. Toda, K. Shimatake, N. Momono, M. Oda, and M. Ido, Phys. Rev. Lett. **101**, 137003 (2008).

[17] D. Pines, Physica C **282**, 273 (1997); Z. Phys. B **103**, 129 (1997).

[18] X.-G. Wen and P. A. Lee, Phys. Rev. Lett. **80**, 2193 (1998).

[19] V. B. Geshkenbein, L. B. Ioffe, and A. I. Larkin, Phys. Rev. B **55**, 3173 (1997).

[20] N. Furukawa, T. M. Rice, and M. Salmhofer, Phys. Rev. Lett. **81**, 3195 (1998).

[21] M. Oda, R. M. Dipasupil, N. Momono, and M. Ido, J. Phys. Soc. Jpn. **69**, 983 (2000).

[22] T. Kurosawa, N. Momono, M. Oda, and M. Ido, Phys. Rev. B. **85**, 134522 (2012).

[23] Y. Toda, T. Mertelj, P. Kusar, T. Kurosawa, M. Oda, M. Ido, and D. Mihailovic, Phys. Rev. B **84**, 174516 (2011).

[24] J. E. Hoffman, K. McElroy, D.-H. Lee, K. M. Lang, H. Eisaki, S. Uchida, and J. C. Davis, Science **297**, 1148 (2002).

[25] K. McElroy, R. W. Simmonds, J. E. Hoffman, D.-H. Lee, K. J. Orenstein, H. Eisaki, S. Uchida, and J. C. Davis, Nature (London) **422**, 592 (2003).

[26] T. Hanaguri, Y. Kohsaka, J. C. Davis, C. Lupien, I. Yamada, M. Azuma, M. Takano, K. Ohishi, M. Ono, and H. Takagi, Nat. Phys. **3**, 865 (2007).

[27] Y. Kohsaka, C. Taylor, P. Wahl, A. Schmidt, J. Lee, K. Fujita, J. W. Alldredge, K. McElroy, J. Lee, H. Eisaki, S. Uchida, D.-H. Lee, and J. C. Davis, Nature (London) **454** 1072 (2008).

[28] K. Fujita, C. K. Kim, I. Lee, J. Lee, M. H. Hamidian, I. A. Firmo, S. Mukhopadhyay, H. Eisaki, S. Uchida, M. J. Lawler, E.-A. Kim, and J. C. Davis, Science **344**, 612 (2014).

[29] Y. He, Y. Yin, M. Zech, A. Soumyanarayanan, M. M. Yee, T. Williams, M. C. Boyer, K. Chatterjee, W. D. Wise, I. Zeljkovic, T. Kondo, T. Takeuchi, H. Ikuta, P. Mistark, R. S. Markiewicz, A. Bansil, S. Sachdev, E. W. Hudson, and J. E. Hoffman, Science **344**, 608 (2014).

[30] K. Fujita, I. Grigorenko, J. Lee, W. Wang, J. X. Zhu, J. C. Davis, H. Eisaki, S. Uchida, and A. V. Balatsky, Phys. Rev. B **78**, 054510 (2008).

[31] T. Hanaguri, Y. Kohsaka, M. Ono, M. Maltseva, P. Coleman, I. Yamada, M. Azuma, M. Takano, K. Ohishi, and H. Takagi, Science **323**, 923 (2009).

[32] T. Machida, Y. Kohsaka, K. Matsuoka, K. Iwaya, T. Hanaguri, and T. Tamegai, Nat. Commun. **7**, 11747 (2016).

[33] K. Fujita, M. H. Hamidian, S. D. Edkins, C. K. Kim, Y. Kohsaka, M. Azuma, M. Takano, H. Takagi, H. Eisaki, S. Uchida, A. Allais, M. J. Lawler, E.-A. Kim, S. Sachdev, and J. C. S. Davis, Proc. Natl. Acad. Sci. USA **111**, E3026 (2014).

[34] M. H. Hamidian, S. D. Edkins, C. K. Kim, J. C. Davis, A. P. Mackenzie, H. Eisaki, S. Uchida, M. J. Lawler, E.-A. Kim, S. Sachdev, and K. Fujita, Nat. Phys. **12**, 150 (2016).

[35] A. Mesaros, K. Fujita, S. D. Edkins, M. H. Hamidian, H. Eisaki, S. Uchida, J. C. S. Davis, M. J. Lawler, and E.-A. Kim, Proc. Natl. Acad. Sci. USA **113**, 12661 (2016).

[36] S. Mukhopadhyay, R. Sharma, C. K. Kim, S. D. Edkins, M. H. Hamidian, H. Eisaki, S. Uchida, E.-A. Kim, M. J. Lawler, A. P. Mackenzie, J. C. S. Davis, and K. Fujita, Proc. Natl. Acad. Sci. USA **116**, 13249 (2019).

[37] T. A. Webb, M. C. Boyer, Y. Yin, D. Chowdhury, Y. He, T. Kondo, T. Takeuchi, H. Ikuta, E. W. Hudson, J. E. Hoffman, and M. H. Hamidian, Phys. Rev. X **9**, 021021 (2019).

[38] Y. Kohsaka, C. Taylor, K. Fujita, A. Schmidt, C. Lupien, T. Hanaguri, M. Azuma, M. Takano, H. Eisaki, H. Takagi, S. Uchida, and J. C. Davis, Science **315**, 1380 (2007).

[39] M. J. Lawler, K. Fujita, J. Lee, A. R. Schmidt, Y. Kohsaka, C. K. Kim, H. Eisaki, S. Uchida, J. C. Davis, J. P. Sethna, and E.-A. Kim, Nature (London) **466**, 347 (2010).

[40] A. Mesaros, K. Fujita, H. Eisaki, S. Uchida, J. C. Davis, S. Sachdev, J. Zaanen, M. J. Lawler, E.-A. Kim, Science **333**, 426 (2011).

[41] Y. Zheng, Y. Fei, K. Bu, W. Zhang, Y. Ding, X. Zhou, J. E. Hoffman, and Y. Yin, Sci. Rep. **7**, 8059 (2017).

[42] J. E. Hoffman, E. W. Hudson, K. M. Lang, V. Madhavan, H. Eisaki, S. Uchida, and J. C. Davis, Science **295**, 466 (2002).

[43] C. Howald, H. Eisaki, N. Kaneko, M. Greven, and A. Kapitulnik, Phys. Rev. B **67**, 014533 (2003).

[44] W. D. Wise, M. C. Boyer, K. Chatterjee, T. Kondo, T. Takeuchi, H. Ikuta, Y. Wang, and E. W. Hudson, Nat. Phys. **4**, 696 (2008).

[45] T. Hanaguri, C. Luplen, Y. Kohsaka, D.-H. Lee, M. Azuma, M. Takano, H. Takagi, and J. C. Davis, Nature (London) **430**, 1001 (2004).

[46] M. Vershinin, S. Misra, S. Ono, Y. Abe, Y. Ando, and A. Yazdani, Science **303**, 1995 (2004).

[47] A. Fang, C. Howald, N. Kaneko, M. Greven, and A. Kapitulnik, Phys. Rev. B **70**, 214514 (2004).

[48] K. McElroy, D.-H. Lee, J. E. Hoffman, K. M. Lang, J. Lee, E. W. Hudson, H. Eisaki, S. Uchida, and J. C. Davis, Phys. Rev. Lett. **94**, 197005 (2005).

[49] N. Momono, A. Hashimoto, Y. Kobatake, M. Oda, and M. Ido, J. Phys. Soc. Jpn. **74**, 2400 (2005).

[50] T. Machida, Y. Kamijo, K. Harada, T. Noguchi, R. Saito, T. Kato, and H. Sakata, J. Phys. Soc. Jpn. **75**, 083708 (2006).

[51] C. V. Parker, P. Aynajian, E. H. da Silva Neto, A. Pushp, S. Ono, J. Wen, Z. Xu, G. Gu, and A. Yazdani, Nature (London) **468**, 677 (2010).

[52] J. W. Alldredge, K. Fujita, H. Eisaki, S. Uchida, and K. McElroy, Phys. Rev. B **85**, 174501 (2012).

[53] E. H. da Silva Neto, P. Aynajian, A. Frano, R. Comin, E. Schierle, E. Weschke, A. Gyenis, J. Wen, J. Schneeloch, Z. Xu, S. Ono, G. Gu, M. Le Tacon, and A. Yazdani, Science **343**, 393 (2014).

[54] R. Comin, A. Frano, M. M. Yee, Y. Yoshida, H. Eisaki, E. Schierle, E. Weschke, R. Sutarto, F. He, A. Soumyanarayanan, Y. He, M. L. Tacon, I. S. Elfimov, J. E. Hoffman, G. A. Sawatzky, B. Keimer, and A. Damascelli, Science **343**, 390 (2014).

[55] T. Kurosawa, K. Takeyama, S. Baar, Y. Shibata, M. Kataoka, S. Mizuta, H. Yoshida, N. Momono, M. Oda, and M. Ido, J. Phys. Soc. Jpn. **85**, 044709 (2016).

[56] M. F. Crommie, C. P. Lutz, and D. M. Eigler, Nature (London) **363**, 524 (1993).

[57] Y. Hasegawa, and Ph. Avouris, Phys. Rev. Lett. **71**, 1071 (1993).

[58] M. Tinkham *Introduction to Superconductivity*, 2nd ed. (McGraw-Hill, New York, 1996).

[59] J. R. Schrieffer, *Theory of Superconductivity* (Perseus, Reading, MA, 1999).

[60] Q.-H. Wang and D.-H. Lee, Phys. Rev. B **67**, 020511 (2003).

[61] R. S. Markiewicz, Phys. Rev. B **69**, 214517 (2004).

[62] T. S. Nunner, W. Chen, B. M. Andersen, A. Melikyan, and P. J. Hirschfeld, Phys. Rev. B **73**, 104511 (2006).

[63] T. Pereg-Barnea, and M. Franz, Phys. Rev. B **78**, 020509 (2008).

[64] M. Maltseva and P. Coleman, Phys. Rev. B **80**, 144514 (2009).

[65] P. Fulde and R. A. Ferrell, Phys. Rev. **135**, A550 (1964).

[66] A. I. Larkin and Y. N. Ovchinnikov, Sov. Phys. JETP. **20**, 762 (1965).

[67] Y. Wang, D. F. Agterberg, and A. Chubukov, Phys. Rev. B **91**, 115103 (2015).

[68] Y. Wang, D. F. Agterberg, and A. Chubukov, Phys. Rev. Lett. **114**, 197001 (2015).

[69] P. A. Lee, Phys. Rev. X **4**, 031017 (2014).

[70] A. Himeda,T. Kato, and M. Ogata, Phys. Rev. Lett. **88**, 117001 (2002).

[71] P. Corboz, T. M. Rice, and M. Troyer, Phys. Rev. Lett. **113**, 046402 (2014).

[72] E. Berg, E. Fradkin, S. A. Kivelson, and J. M. Tranquada, New J. Phys. **11**, 115004 (2009).

[73] H. D. Chen, O. Vafek, A. Yazdani, and S. C. Zhang, Phys. Rev. Lett. **93**, 187002 (2004).

[74] K. Seo, H. D. Chen, and J. P. Hu, Phys. Rev. B **78**, 094510 (2008).

[75] C. Pépin, V. S. de Carvalho, T. Kloss, and X. Montiel, Phys. Rev. B

**90**, 195207 (2014).

[76] H. Freire, V. S. de Carvalho, and C. Pépin, Phys. Rev. B **92**, 045132 (2015).

[77] M. H. Hamidian, S. D. Edkins, S. H. Joo, A. Kostin, H. Eisaki, S. Uchida, M. J. Lawler, E.-A. Kim, A. P. Mackenzie, K. Fujita, J. Lee, and J. C. S. Davis, Nature (London) **532**, 343 (2016).

[78] E. Fradkin, S. A. Kivelson, and J. M. Tranquada, Rev. Mod. Phys. **87**, 457 (2015).

[79] D. F. Agterberg, J. C. S. Davis, S. D. Edkins, E. Fradkin, D. J. Van Harlingen, S. A. Kivelson, P. A. Lee, L. Radzihovsky, J. M. Tranquada, and Y. Wang, Annu. Rev. Condens. Matter Phys. **11**, 231 (2020).

[80] S. D. Edkins, A. Kostin, K. Fujita, A. P. Mackenzie, H. Eisaki, S. Uchida, S. Sachdev, M. J. Lawler, E.-A. Kim, J. C. S. Davis, M. H. Hamidian, Science **364**, 976 (2019).

[81] Z. Du, H. Li, S. H. Joo, E. P. Donoway, J. Lee, J. C. S. Davis, G. Gu, P. D. Johnson, and K. Fujita, Nature (London) **580**, 65 (2020).

[82] W. Ruan, X. Li, C. Hu, Z. Hao, H. Li, P. Cai, X. Zhou, D.-H. Lee, and Y. Wang, Nat. Phys. **14**, 1178 (2018).

[83] D. L. Feng, D. H. Lu, K. M. Shen, C. Kim, H. Eisaki, A. Damascelli, R. Yoshizaki, J.-i. Shimoyama, K. Kishio, G. D. Gu, S. Oh, A. Andrus, J. O'Donnell, J. N. Eckstein, and Z.-X. Shen, Science **289**, 277 (2000).

[84] K. K. Gomes, A. N. Pasupathy, A. Pushp, S. Ono, Y. Ando, and A. Yazdani, Nature **447**, 569 (2007).

[85] S. H. Pan, E. W. Hudson, K. M. Lang, H. Eisaki, S. Uchida, and J. C. Davis, Nature **403**, 746 (2000).

[86] S. H. Pan, E. W. Hudson, A. K. Gupta, K.-W. Ng, H. Eisaki, S. Uchida, and J. C. Davis, Phys. Rev. Lett. **85**, 1536 (2000).

[87] S. Takekawa, H. Nozaki, A. Umezono, K. Kosuda, and M. Kobayashi, J. Cryst. Growth **92**, 687 (1988).

[88] I. Shigaki, K. Kitahama, K. Shibutani, S. Hayashi, R. Ogawa, Y. Kawate, T. Kawai, S. Kawai, M. Matsumoto, and J. Shirafuji, Jpn. J. Appl. Phys. **29**, L2013 (1990).

[89] W. A. Groen, D. M. de Leeuw, and L. F. Feiner, Physica C **165**, 55 (1990).

[90] G. Binnig and H. Rohrer, Surface Science **126**, 236 (1983).

[91] J. Bardeen, Phys. Rev. Lett. **6**, 57 (1961).

[92] J. Tersoff and D. R. Hamann, Phys Rev. Lett. **50**, 1998 (1983).

[93] J. Tersoff and D. R. Hamann, Phys Rev. B **31**, 805 (1985).

[94] C. J. Chen, *Introduction to Scanning Tunneling microscopy*, 2nd ed. (Oxford University Press, Oxford, 2008).

[95] A. J. Macdonald, Y.-S. Tremblay-Johnston, S. Grothe, S. Chi1, P. Dosanjh, S. Johnston, and S. A. Burke, Nanotechnology **27**, 414004 (2016).

[96] A. Hashimoto, N. Momono, M. Oda, and M. Ido, Phys. Rev. B **74**, 064508 (2006).

[97] T. Kurosawa, T. Yoneyama, Y. Takano, M. Hagiwara, R. Inoue, N. Hagiwara, K. Kurusu, K. Takeyama, N. Momono, M. Oda, and M. Ido, Phys. Rev. B **81**, 094519 (2010).

[98] I. M. Vishik, M. Hashimoto, R.-H. He, W.-S. Lee, F. Schmitt, D. Lu, R. G. Moore, C. Zhang, W. Meevasana, T. Sasagawa, S. Uchida, K. Fujita, S. Ishida, M. Ishikado, Y. Yoshida, H. Eisaki, Z. Hussain, T. P. Devereaux, and Z.-X. Shen, Proc. Natl. Acad. Sci. USA **109**, 18332 (2012).

[99] I. Martin, A.V. Balatsky, and J. Zaanen, Phys. Rev. Lett. **88**, 097003 (2002).